



Photocurrent generation with two-dimensional van der Waals semiconductors.

Journal:	<i>Chemical Society Reviews</i>
Manuscript ID:	CS-SYN-02-2015-000106.R3
Article Type:	Review Article
Date Submitted by the Author:	13-Apr-2015
Complete List of Authors:	<p>Buscema, Michele; Delft University of Technology, Kavli Institute of Nanoscience Island, Joshua; Delft University of Technology, Kavli Institute of Nanoscience Groenendijk, Dirk; Delft University of Technology, Kavli Institute of Nanoscience Blanter, Sofya; University of Regensburg, Institute for Experimental and Applied Physics Steele, G. A. ; Delft University of Technology, Kavli Institute of Nanoscience van der Zant, Herre; Delft University of Technology, Kavli Institute of Nanoscience Castellanos-Gomez, Andres; Delft University of Technology, Kavli Institute of Nanoscience; Instituto Madrileño de Estudios Avanzados en Nanociencia (IMDEA-Nanociencia),</p>

Photocurrent generation with two-dimensional van der Waals semiconductors

Michele Buscema,^{*a} Joshua O. Island,^a Dirk J. Groenendijk,^a Sofya I. Blanter,^{a,b} Gary A. Steele,^a Herre S.J. van der Zant^a, and Andres Castellanos-Gomez^{*a,c}

Received Xth XXXXXXXXXXXX 20XX, Accepted Xth XXXXXXXXXXXX 20XX

First published on the web Xth XXXXXXXXXXXX 200X

DOI: 10.1039/b000000x

Two-dimensional (2D) materials have attracted a great deal of interest in recent years. This family of materials allows for the realization of versatile electronic devices and holds promise for next-generation (opto)electronics. Their electronic properties strongly depend on the number of layers, making them interesting from a fundamental standpoint. For electronic applications, semiconducting 2D materials benefit from sizable mobilities and large on/off ratios, due to the large modulation achievable via the gate field-effect. Moreover, being mechanically strong and flexible, these materials can withstand large strain (> 10%) before rupture, making them interesting for strain engineering and flexible devices. Even in their single layer form, semiconducting 2D materials have demonstrated efficient light absorption, enabling large responsivity in photodetectors. Therefore, semiconducting layered 2D materials are strong candidates for optoelectronic applications, especially for photodetection. Here, we review the state-of-the-art in photodetectors based on semiconducting 2D materials, focusing on the transition metal dichalcogenides, novel van der Waals materials, black phosphorus, and heterostructures.

1 Introduction

Photodetectors are a key component of many devices we use in our daily life. From imaging to optical communications, we rely on photodetectors to convert the information stored in light into electrical signals that can be processed by standard electronics. Silicon photodetectors are readily integrated in complementary metal-oxide-semiconductor (CMOS) technology, profiting from device miniaturization and scalability which considerably reduce costs and expand the range of applications.

Bulk Silicon photodetectors suffer from the limitations of silicon as a light-absorbing material. Its indirect bandgap of about 1.1 eV limits absorption to the visible and near-infrared part of the electromagnetic spectrum and reduces its efficiency. To achieve sizable responsivities, photodetectors based on bulk silicon rely on a thick channel, making the photodetector fully opaque. Silicon is also a brittle material in bulk, precluding its use in bendable device concepts. Other 3D materials, like InGaAs and related heterostructures, are also currently employed in photodetectors. While they allow efficient detection of IR wavelengths, they share most of silicon drawbacks and add a sizable increase in cost due to fabrication

complexity.

Novel, nanoscale semiconducting materials are needed to overcome the limitation of bulk silicon for photodetection. For instance, nanostructured silicon¹ and especially Si nanowires² have shown in the past years the possibility to realize bendable and transparent devices. More recently, silicene (a single layer of silicon atoms) has been successfully used to fabricate FETs, opening the door to the study its optoelectronic properties.³

These new materials should provide higher absorption efficiencies in the visible, an extended operation wavelength range, fast detection and, preferably, facile integration with current CMOS technology for readout.

The large class of semiconducting layered materials presents appealing properties such as high transparency (and yet strong light-matter interaction), flexibility and ease of processing. Therefore, they recently attracted a large research effort aimed at understanding the principal photodetection mechanisms and device performances.

The isolation of graphene in 2004,^{4,5} rapidly followed by the discovery of its amazing properties,^{6–13} has generated an intense research effort on layered 2D materials.^{6,14} In layered 2D materials, the atoms forming the compound are arranged into planes (layers) that are held together by strong in-plane bonds, usually covalent. To form a 3D crystal, the atomic layers are stacked in the out-of-plane direction with weak van der Waals interactions. This allows the exfoliation of bulk crystals and the fabrication of thinner *flakes*, even down to the single

^a Kavli Institute of Nanoscience, Delft University of Technology, Lorentzweg 1, 2628 CJ, Delft, The Netherlands. E-mail: m.buscema@tudelft.nl ^b Current address: Institute for Experimental and Applied Physics, University of Regensburg, 93040 Regensburg, Germany. ^c Current address: Instituto Madrileño de Estudios Avanzados en Nanociencia (IMDEA-Nanociencia), 28049 Madrid, Spain. E-mail: andres.castellanos@imdea.org

layer limit.⁵

Flakes of layered materials present several advantages over conventional 3D materials for photodetection, from both a practical and a fundamental standpoint. The atomic thickness renders these materials almost transparent, which is of high interest for novel applications, e.g. photovoltaics integrated in façades or wearable electronics. Their atomic thickness is also responsible for quantum confinement effects in the out-of-plane direction. These effects are particularly strong in the semiconducting transition metal dichalcogenides - TMDCs - where the reduced thickness results in strongly bound excitons, increasing the absorption efficiency.^{15–17} Another effect of the vertical confinement is the modulation of the bandgap as a function of the number of layers, particularly evident in TMDCs,^{15,18–22} which modulates the optical absorption edge.

In two-dimensional semiconductor crystals, the electronic bands are localized in nature (due to the *d* orbital contribution), leading to sharp peaks in the density of states at a particular energy (i.e. Van Hove singularities)²³. In several 2D semiconductors (for instance MoS₂, WS₂ and WSe₂) these singularities happen close to the conduction and valence band edges. Therefore, a photon with energy close to the bandgap has an increased probability to excite an electron-hole pair due to the large availability of empty states given by the diverging DOS at the singularity. Thus, despite of the reduced thickness of 2D semiconductors (yielding the high transparency) they strongly interact with the incident light.

2D materials have also demonstrated remarkable elastic modulus and large strain (> 10%) before rupture. Large strains have a strong effect on the electronic and optical behavior of these materials.^{9,22,24–27} Thus, strain-engineering can be used to tune the optical properties and realize novel device architectures (wearable, bendable devices) and devices with novel functionalities, like exciton funnelling.^{28,29}

In this Review, we present the state-of-art in photodetection with layered materials, especially focusing on the semiconducting 2D materials. For the purpose of this review, we consider as two dimensional the materials in which (i) the atoms have strong in-plane bonds, (ii) the atoms are arranged into planes with high crystalline order and (iii) these atomically-thin planes are held together only by van der Waals interactions in the vertical direction (i.e. there are no dangling bonds at the surfaces of the planes). The absence of dangling bonds between the planes and the weak van der Waals interaction makes it possible to isolate single-unit-cell-thickness flakes by mechanical exfoliation of a parent, bulk crystal. They also allow stacking several layers of different materials on top of each other and to grow them on a variety of substrates, while still preserving the high crystalline order. These are all properties in stark contrast with conventional 3D crystalline materials. Layered materials, even when relatively thick (~ 10 nm) compared to a single layer, already possess a strong in-plane

vs out-of-plane anisotropy in their properties. Further thickness reduction to a small number of layers, ultimately to a single layer, also induces quantum confinement in the vertical direction, which has a strong impact on the bandgap of the material. This effect is particularly strong in the TMDCs, whose bandgap increases and becomes direct in single layer, and black phosphorus, whose bandgap increases of more than 3 times. In the following, we review devices based on flakes with thickness from one unit cell to several nanometers and with in-plane dimensions in the order of microns.

We start by briefly introducing the main photodetection mechanisms and figures-of-merit that are useful to compare different photodetectors. We then move on to describe photodetectors based on semiconducting transition metal dichalcogenides (TMDCs). Next, we summarize the performance of photodetectors based on the novel van der Waals materials, such as Ga, In and Sn chalcogenides and Ti, Hf and Zr trichalcogenides. Then we describe the recent progress in black phosphorus-based photodetectors. We then briefly compare the responsivity and time response of the reviewed detectors. Subsequently, we describe one of the future directions of photodetection with layered materials: van der waals heterostructures. Finally, we summarize the main conclusions of this Review and list future challenges.

2 Photocurrent generation mechanisms

This Section briefly introduces the mechanisms enabling photodetection. We start by describing the mechanisms driven by electric field separation of electron-hole pairs generated by photon absorption. These mechanisms are usually categorized as photoconduction, photogating and the photovoltaic effect and are especially relevant for (photo)-field-effect transistors (FETs). Next, we introduce thermal processes (photo-thermoelectric, bolometric) that can also generate or modulate the photoresponse in photodetectors. At last, we discuss the relevant figures-of-merit for photodetectors to facilitate comparison among devices working with different principles.

2.1 Photocurrent generation driven by electron-hole separation

2.1.1 Photoconductive effect. In the photoconductive effect, photon absorption generates extra free carriers, reducing the electrical resistance of the semiconductor (see Figure 1).^{30–33} Figure 1a sketches the band diagram of an FET. Without illumination and under an applied bias (V_{ds}), a small source-drain current can flow (I_{dark}). Under illumination, the absorption of photons with energy higher than the bandgap ($E_{ph} > E_{bg}$) generates e-h pairs which are separated by the applied V_{ds} (Figure 1b). The photogenerated free electrons and

holes drift in opposite directions towards the metal leads, resulting in a net increase in the current (I_{photo}). This photogenerated current adds to the dark current, reducing the resistance of the device, as depicted in Figure 1c and Figure 1d.

It is instructive to consider the case of a large difference between the electron and hole mobilities, resulting in a large difference in the electron/hole transit time (τ_{transit}):³²

$$\tau_{\text{transit}} = \frac{L^2}{\mu \cdot V_{\text{ds}}}, \quad (1)$$

where L is the length of the transistor channel, μ the charge carrier mobility and V_{ds} the source-drain bias. If the hole mobility is much lower than the electron mobility, the photogenerated electrons can cross the channel much faster than the photogenerated holes. Until recombination or hole extraction, many electrons can participate in the photocurrent, leading to the photoconductive gain (G). Effectively, this means that more electrons can be extracted from a single photon, resulting in a quantum efficiency larger than one. The photoconductive gain is the ratio of the photogenerated carrier lifetime ($\tau_{\text{photocarriers}}$) and the transit time:³²

$$G = \frac{\tau_{\text{photocarriers}}}{\tau_{\text{transit}}} = \frac{\tau_{\text{photocarriers}} \cdot \mu \cdot V}{L^2}. \quad (2)$$

Hence, large $\tau_{\text{photocarriers}}$ and a large mismatch in the electron/hole mobility yield large G .

Photogating is a particular example of the photoconductive effect. If holes/electrons are *trapped* in localized states (see Figure 2a), they act as a local gate, effectively modulating the resistance of the material. In this case, $\tau_{\text{photocarriers}}$ is only limited by the recombination lifetime of the localized *trap* states, leading to a large G .³² The trap states where carriers can reside for long times are usually located at defects or at the surface of the semiconducting material. This effect is of particular importance for nanostructured materials, like colloidal quantum dots, nanowires and two dimensional semiconductors, where the large surface and reduced screening play a major role in the electrical properties.

Photogating can be seen as a horizontal shift in the $I_{\text{ds}}-V_{\text{g}}$ traces under illumination, as shown schematically in Figure 2. Under illumination, the absorption of a photon generates an e-h pair. One carrier type (holes in Figure 2b) is then trapped in localized states with energy near the valence band edge. In this case, the electric field-effect of the trapped holes shifts the Fermi level which, in turn, induces more electrons. The increased electron density reduces the resistance of the device, allowing more current to flow (I_{photo}). Under illumination, the $I_{\text{ds}}-V_{\text{g}}$ trace will be horizontally shifted (ΔV_{g}) with respect to the dark trace due to the effective gate electric field of the trapped charges. The sign of ΔV_{g} indicates the polarity of the trapped carrier. Photogating can also result in a negative I_{photo} , as sketched in Figure 2c,d.

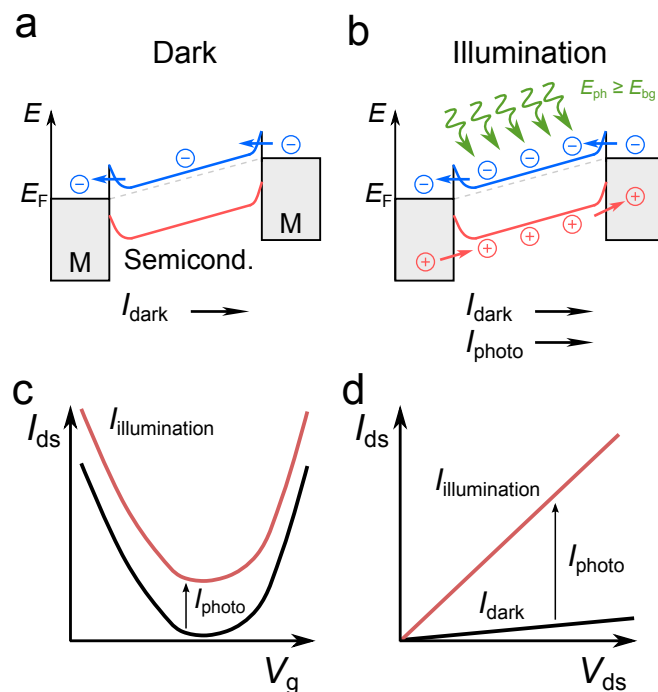


Fig. 1 Schematic of the photoconductive effect. (a) Band alignment for a semiconductor channel contacted with two metals (M) under an external bias without illumination. A small current flows through the device (I_{dark}). (b) Band alignment under illumination with photons of energy (E_{ph}) higher than the bandgap (E_{bg}). The absorption of photons generates e-h pairs that are separated by the external applied bias, generating a photocurrent (I_{photo}) which adds to I_{dark} . (c) $I_{\text{ds}}-V_{\text{g}}$ traces in the dark (solid black line) and under illumination (solid red line). Illumination results in an increase in the conductivity (vertical shift) and a positive photocurrent across the entire gate voltage range. (d) $I_{\text{ds}}-V_{\text{ds}}$ curves in the dark (solid black line) and under illumination (solid red line). Illumination results in an increase in the conductivity and a positive photocurrent.

In practice, the clear distinction between photoconductive and photogating effect is faded, since both effects can take place in the same device. However, the difference in their time scales can be used to disentangle their signatures, as shown by Furchi *et al.*³⁴

2.1.2 Photovoltaic effect. In the photovoltaic effect, photogenerated e-h pairs are separated by an *internal* electric field. The origin of the internal electric field could be a PN junction or a Schottky barrier at the interface between a semiconductor and a metal (see Figure 3a).³² In both cases, the devices present nonlinear $I_{\text{ds}}-V_{\text{ds}}$ characteristics in the dark. In the case of PN junctions, the forward source-drain current I_{ds} is exponential with the source-drain voltage V_{ds} as $I_{\text{ds}} \propto \exp(V_{\text{ds}}) - 1$; the reverse current, on the other hand, is

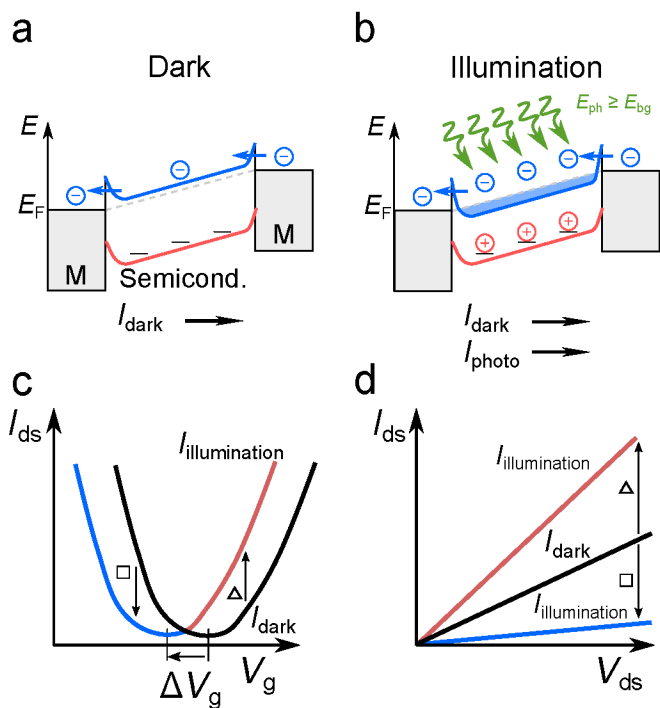


Fig. 2 Photogating schematics. (a) Band alignment for a semiconductor channel contacted with two metals (M) under external bias in the dark. A small electron current flows through the device (I_{dark}). The solid horizontal solid segments represent trap states at the valence band edge. (b) Band alignment under illumination with photons of energy (E_{ph}) higher than the bandgap (E_{bg}). The absorption of a photon generates an electron-hole pair. Holes are trapped at the band edge and act as a local gate. The field-effect induces more electrons in the channel, generating a photocurrent (I_{photo}) which adds to the I_{dark} . (c) $I_{\text{ds}}-V_{\text{g}}$ traces in the dark (solid black line) and under illumination (solid blue/red line). Illumination results in a horizontal shift (ΔV_{g}) of the traces, due to the trapped charges that act as an additional gate electric field. (d) $I_{\text{ds}}-V_{\text{ds}}$ curves in dark (solid black line) and under illumination at the gate value marked by a triangle in panel c (solid red line) and at the gate voltage marked by a square in panel c (solid blue line). Illumination results in positive photocurrent for one gate value (triangle marker) and negative photocurrent for another gate value (square marker).

negligibly small until junction breakdown.³⁵ Under illumination and zero external bias ($V_{\text{ds}} = 0$), the internal electric field separates the photoexcited e-h pairs thereby generating a sizable photocurrent (short-circuit current, I_{sc}). Keeping the circuit open leads to the accumulation of carriers of opposite polarities in distinct parts of the device, thereby generating a voltage (open circuit voltage, V_{oc}). Under illumination and reverse bias, the magnitude of the reverse current increases since the photoexcited carriers are swept in opposite directions by

the junction electric field. An additional forward-bias is required to compensate the photogenerated reverse-current, also justifying a non-zero V_{oc} . In contrast to the photoconductive effect, the photovoltaic effect can also be used to convert the energy of the photons to electrical energy.

Figure 3b plots the $I_{\text{ds}}-V_{\text{ds}}$ characteristics of a PN junction in the dark (black solid line) and under illumination (red line). Since the photocurrent has the same sign as the reverse current, the $I_{\text{ds}}-V_{\text{ds}}$ under illumination appears shifted downwards, with respect to the dark curve. The part of the $I_{\text{ds}}-V_{\text{ds}}$ curve that lays in the fourth quadrant (negative current, positive bias) is used to generate electrical power ($P_{\text{el}}^{\text{max}}$).

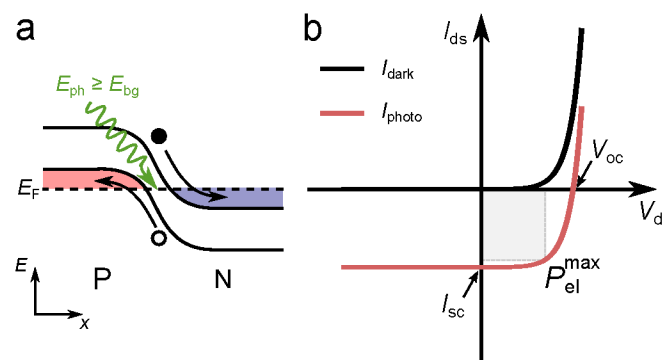


Fig. 3 Photovoltaic effect schematics. (a) Band alignment in a PN junction. The dashed line represents the common Fermi energy (E_{F}) for the P-doped and N-doped semiconductor. The absorption of a photon with $E_{\text{ph}} > E_{\text{bg}}$ generates an electron-hole (black dot and white dot respectively) pair. The electron-hole pair is then separated and accelerated by the built-in electric field at the junction. (b) $I_{\text{ds}}-V_{\text{ds}}$ curves in the dark (solid black line) and under illumination (solid red line). The illumination results in a short-circuit current I_{sc} and an open-circuit voltage V_{oc} . The device produces electrical power when operated in the fourth quadrant. The point of maximum power generation is indicated as $P_{\text{el}}^{\text{max}}$.

Photodetectors based on the photovoltaic effect are usually PN diodes and are used at zero bias (photovoltaic mode) or under reverse bias (photoconductive mode). In the photovoltaic mode, the dark current is the lowest, improving the detectivity (see Section 3) of the detector. However, the absolute responsivity (see Section 3) is usually smaller than a photodetector working with the photoconducting or photogating mechanism, since there is no internal gain. The advantage of reverse-bias operation (the photoconductive mode) is the reduction of the junction capacitance, increasing the speed of the photodiode. Under large reverse bias, the strong junction electric field can give enough energy the photogenerated electrons to initiate impact ionization multiplications, or avalanching (avalanche photodiode - APD). This mechanism provide large internal gain, so that light of extremely low power can be detected.

2.1.3 Simplified photocurrent generation phenomenological description. The generated photocurrent, I_{photo} , in a photoconductive detector can be estimated with the following phenomenological formula:

$$I_{\text{photo}} = I_{\text{illumination}} - I_{\text{dark}} = \Gamma \cdot \eta \cdot e \cdot G, \quad (3)$$

where Γ is the number of absorbed photons per unit time, η the efficiency of the conversion of the absorbed photons to electrons, e the electron charge and G is the photoconductive gain. The parameter η is the internal quantum efficiency of the detector, without considering gain mechanisms. For a photo-voltaic detector $G = 0$.

With the help of Equation 2, we can now rewrite Equation 3 as:³⁶

$$I_{\text{photo}} = \Gamma \cdot \eta \cdot e \cdot G \frac{\tau_{\text{photocarriers}} \cdot \mu \cdot V}{L^2}. \quad (4)$$

From this Equation we see that I_{photo} is linearly dependent on the photon flux (i.e. the excitation power), the photogenerated carrier lifetime, the electron mobility and the applied bias, following simple physical intuition.

This simplified model, however, does not take into account the presence of a finite number of trap states. These trap states strongly affect the dependence of the photocurrent on the excitation power (usually it becomes sub-linear) and the carrier lifetime (usually it increases). Engineering trap states is a viable way to achieve ultra high gain, usually at the expense of a slower time response of the detector.

2.2 Photocurrent generation driven by thermal mechanisms

Temperature *gradients* induced by non-uniform heating under illumination can also generate a photocurrent or photovoltage through the photo-thermoelectric effect. On the other hand, a *homogeneous* temperature change affects the resistivity of a material (photo-bolometric effect), which can be detected by electrical means.

2.2.1 Photo-thermoelectric effect. In the photo-thermoelectric effect (PTE), a heat gradient from light-induced heating results in a temperature gradient across a semiconductor channel. As a result, the two ends of the semiconductor channel display a temperature difference ΔT . This ΔT is converted into a voltage difference ΔV via the Seebeck (or thermoelectric) effect (see Figure 4). The magnitude of ΔV is linearly proportional to the temperature gradient via the Seebeck coefficient (S):³⁷

$$\Delta V = S \cdot \Delta T. \quad (5)$$

The heat gradient can stem from either localized illumination, as with a focused laser spot with dimensions much smaller

than those of the measured device,^{38,39} or from a strong difference in the absorption in distinct parts of the device under global illumination.⁴⁰

The origin of the Seebeck effect can be found in three main microscopic processes, in dynamic equilibrium with each other.^{37,41} Relating the Seebeck coefficient to microscopic quantities is, however, difficult. Therefore, the Seebeck coefficient is usually expressed in terms of the conductivity of the material through the Mott relation:^{42–45}

$$S = \frac{\pi^2 k_B^2 T}{3e} \left. \frac{d \ln(\sigma(E))}{dE} \right|_{E=E_F}, \quad (6)$$

where k_B is the Boltzmann constant and $\sigma(E)$ the conductivity as a function of energy (E), and where the derivative is evaluated at the Fermi energy, E_F . The sign of the Seebeck coefficient is determined by the majority charge carrier polarity in the semiconductor.

Through the photo-thermoelectric effect (PTE), a temperature gradient generates a voltage difference that can drive a current through a device at zero V_{ds} . As sketched in Figure 4, a device which is illuminated by a focused laser spot can be modeled as two junctions between the contact metal and the semiconductor channel. In this example, a focused illumination on one of the electrical contacts keeps a steady-state temperature difference (ΔT) between the two junctions, leading to a voltage difference across them (ΔV_{PTE}):

$$\Delta V_{\text{PTE}} = (S_{\text{semiconductor}} - S_{\text{metal}}) \cdot \Delta T \approx S_{\text{semiconductor}} \cdot \Delta T. \quad (7)$$

In Equation 7, the term $S_{\text{metal}} \cdot \Delta T$ can usually be neglected because the Seebeck coefficients of pure metals are in the order of $1 \mu\text{V K}^{-1}$, much smaller than typical values for semiconductors, reported in Table 1. ΔT can be estimated via finite element simulations^{39,46,47} or measured with on-chip thermometers.^{47,48} Once ΔT is known, it is possible to estimate the Seebeck coefficient of the semiconductor material. Seebeck coefficient values for common materials are listed in Table 1. The magnitude of ΔV_{PTE} typically ranges from tens of μV to tens of mV. In order to drive current through the device, the electrodes metals need to form ohmic contacts to the semiconductor. In case the illumination is focussed on a uniform semiconducting channel, no current will flow in the device since no external bias is applied and negligible thermal gradients can be achieved.

Figure 4 shows a typical $I_{\text{ds}} - V_{\text{ds}}$ curve of a device where the photoresponse is dominated by the photo-thermoelectric effect. In the dark, the I_{ds} is linear with the V_{ds} indicating that the Schottky barriers are small (ohmic contact). Under illumination, the photo-thermoelectric effect generates a current at zero bias, without changing the resistance of the device. ΔV_{PTE} can be read off from the intersection with the zero-current axis, as illustrated in Figure 4.

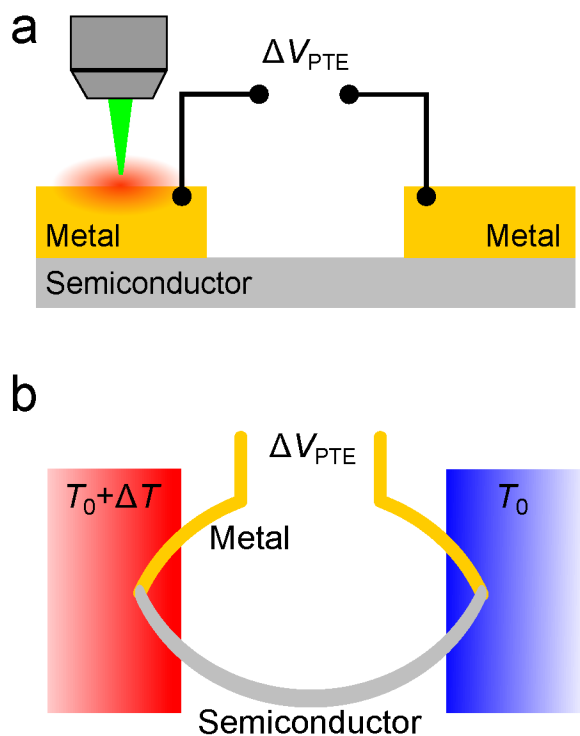


Fig. 4 Photo-thermoelectric effect. (a) Schematic of a field-effect transistor locally illuminated by a focused laser spot on one of the metal contacts to the semiconducting channel. The circuit is open and a thermoelectric voltage ΔV_{PTE} develops across the contacts. (b) Thermal circuit corresponding to the device depicted in (a). The two metal/semiconductor junctions are kept at a steady-state temperature difference ΔT , generating a photo-thermoelectric voltage ΔV_{PTE} . (c) $I_{\text{ds}}-V_{\text{ds}}$ characteristics in the dark (black solid line) and under illumination (red solid line) of a device whose photoresponse is dominated by the photo-thermoelectric effect. Illumination results in a current at zero bias and a thermoelectric voltage ΔV_{PTE} across the contacts when the circuit is kept open.

2.2.2 Photo-bolometric effect. The photo-bolometric effect (PBE) is based on the change of resistivity of a material due to uniform heating induced by photon absorption. The magnitude of this effect is proportional to the conductance variation of a material with temperature (dG/dT) and the homogeneous temperature increase (ΔT) induced by laser heating. The bolometric effect underpins many detectors for mid and far-IR.⁶² Detectors working on this principle usually operate in a four-wire configuration to increase the accuracy in the determination of the conductance change. Recent reports have also demonstrated the importance of the photo-bolometric effect for graphene-based detectors, where electron cooldown is limited by the available phonons,^{63,64} and for photodetectors

Material	Seebeck coefficient ($\mu\text{V K}^{-1}$)	Ref
Graphene	± 4 to ± 100	49–53
CNT	~ 300	54
Organic Semicond.	1×10^3	55
Bi_2Te_3	± 150	56,57
MnO_2	$\sim 4 \times 10^4$	58
Fe_2O_3	$\sim 1 \times 10^4$	59
MoS_2	1×10^5	39
MoS_2	3×10^4	48
Black phosphorus	60	60
Black phosphorus	335	61

Table 1 Seebeck coefficients of some thermoelectric materials.

based on ~ 100 nm thick black phosphorus.^{65,66}

2.2.3 Comparison between photo-thermoelectric and bolometric effects. The main difference between the PTE and the PBE is that the PBE cannot drive currents in a device. Since the PBE is related to a change in the conductivity of the material with temperature, it will only modify the magnitude of the current flowing under external bias and illumination.

The sign of the photoresponse is also very different between the two mechanisms. In the PTE, the sign of the photocurrent is related to the difference in Seebeck coefficients between the components of the junction and, ultimately, to the type of charge carriers in the semiconductor material. For the PBE, the sign of the photocurrent is related to the change in the material conductivity with temperature.⁶²

From a device architecture perspective, the photo-thermoelectric effect requires a temperature difference between two junctions of materials with different Seebeck coefficients. In contrast, the photo-bolometric effect will be present in a homogeneous material, with a homogeneous temperature profile, and under external bias.

3 Photodetectors figures-of-merit

To facilitate comparison between photodetectors working with different principles and realized with different materials and geometries, it is customary to use a set of figures-of-merit. In the following discussion, we will briefly introduce the general meaning of each figure of merit and give a reference to commercial silicon and InGaAs photodetectors and also recent graphene-based detectors, as a benchmark.

Responsivity, \mathcal{R} , measured in A W^{-1} . The responsivity is the ratio between the photocurrent and the total incident optical power on the photodetector. It is an indication of the achievable electrical signal under a certain illumination power: a large responsivity indicates a large electrical output

signal for a defined optical excitation power. With the help of Equation 4, we can define the responsivity as:

$$\begin{aligned} \mathfrak{R} &= \frac{I_{\text{photo}}}{P} = \Gamma \eta e G \cdot \frac{\tau_{\text{photocarriers}} \mu V}{L^2} \cdot \frac{\lambda}{\Gamma_{\text{total}} hc} = \\ &= \frac{\Gamma e \lambda}{\Gamma_{\text{total}} hc} \cdot \eta \cdot G \cdot \tau_{\text{photocarriers}} \cdot \frac{\mu V}{L^2}, \end{aligned} \quad (8)$$

where λ is the photon wavelength, h Planck's constant, c the speed of light in vacuum and Γ_{total} is the total photon flux. Equation 8 shows that the responsivity still depends on the external bias (V) or geometrical factors, at least in the simplified model presented here. For commercial silicon photodiodes, the responsivity is in the order of 500 mA W^{-1} at a wavelength of 880 nm and becomes negligible for wavelengths shorter than 405 nm and larger than 1100 nm. Commercial InGaAs detectors reach $\sim 1.2 \text{ A W}^{-1}$ at $\lambda = 1550 \text{ nm}$. For graphene photodetectors, the responsivity is about 10 mA W^{-1} across the visible and telecommunication wavelengths.¹⁰ Recently, more complex graphene detectors based on photogating either with quantum dots⁶⁷ or with another graphene sheet separated by a tunnel barrier⁶⁸ have achieved much larger responsivities: $1 \times 10^7 \text{ A W}^{-1}$ and $1 \times 10^3 \text{ A W}^{-1}$, respectively.

External quantum efficiency, EQE, dimensionless. The external quantum efficiency is the ratio of the number of the charge carriers in the photocurrent n_e and the total number of impinging excitation photons $n_{\text{photon}}^{\text{total}}$. It is closely related to the responsivity \mathfrak{R} :

$$EQE = \frac{n_e}{n_{\text{photon}}^{\text{total}}} = \mathfrak{R} \cdot \frac{hc}{e\lambda}, \quad (9)$$

The *EQE* is a measure of the optical gain G in the photodetector: $EQE > 1$ effectively means that more than one charge carrier per impinging photon is measured. It is usually a lower bound for the internal quantum efficiency since it assumes that all the incident photons are absorbed. For a silicon photodiode the *EQE* is in the order of 6×10^5 and for a graphene detector is about 1×10^{-2} .^{10,69}

Internal quantum efficiency, IQE = η , dimensionless. The internal quantum efficiency is number of measured charge carriers n_e divided by the number of *absorbed* photons $n_{\text{photon}}^{\text{abs}}$:

By accounting for the photon losses due to transmission and, for a small part, reflection, it is possible to determine the amount of absorbed photons and calculate the internal quantum efficiency. Compared to their bulk counterparts, ultrathin layered materials have an increased photon loss due to transmission. Therefore, at the same *EQE*, ultrathin layered materials have a larger *IQE*. To give a correct estimate of the absorbed photons, optical interference effects should be considered. These effects can enhance photon absorption up to 10% \sim 15%.^{70–72}

Time response, measured in s. The time response of a photodetector is usually measured between 10% and 90% of the generated signal under modulated excitation intensity, either on the raising or falling edge. A photodetector with a small response time is usually desired to allow for certain applications, like video-rate imaging. Commercial silicon and InGaAs photodiodes show rise times of about 50 ps while graphene detectors can already reach hundreds of picoseconds.^{10,69}

Bandwidth, B, measured in Hz. The bandwidth of a photodetector is defined as the modulation frequency ($f_{\text{modulation}}$) of the incoming light excitation at which the intensity of the detector signal is 3 dB less than under continuous illumination. A photodetector with a large bandwidth is desirable for high-rate optical information transfer. As for the response time, the bandwidth of commercial silicon and graphene detectors is similar and reaches a few tens GHz.^{10,69} Using optical correlation techniques, the intrinsic bandwidth of graphene has been estimated to be about 260 GHz.⁷³

Noise equivalent power, NEP, measured in $\text{W Hz}^{-\frac{1}{2}}$. The noise equivalent power is the minimum illumination power that delivers a unity signal-to-noise ratio at 1 Hz bandwidth. It is similar to the *sensitivity* figure-of-merit for other type of detectors. It is a measure of the minimum detectable illumination power; thus a low *NEP* is a desirable property of a photodetector. It can be estimated by:

$$NEP = \frac{PSD}{\mathfrak{R}}, \quad (10)$$

where the *PSD* is the current noise power spectral density in dark (in $\text{A Hz}^{-\frac{1}{2}}$) at 1 Hz bandwidth. Under the assumption of a shot-noise limited detector, the *PSD* is proportional to the square root of the dark current. Thus a detector with a small dark current and large responsivity will have a small *NEP*. Commercial silicon photodiodes have a *NEP* in the order of $1 \times 10^{-14} \text{ W Hz}^{-\frac{1}{2}}$, InGaAs detectors reach one order of magnitude lower, and graphene detectors show values about $1 \times 10^{-12} \text{ W Hz}^{-\frac{1}{2}}$, being limited by the high dark current.

Detectivity, D^ , measured in $\frac{\text{cm}\sqrt{\text{Hz}}}{\text{W}}$.* The detectivity (D^*) is a figure-of-merit derived from the *NEP*, area and bandwidth that enables comparison between photodetectors of different geometries: a higher detectivity indicates a better photodetector performance. It is defined as:

$$D^* = \frac{\sqrt{AB}}{NEP} \quad (11)$$

where A is the area of the photodetector and B is its bandwidth. The detectivity of silicon photodiodes is in the order of $1 \times 10^{12} \frac{\text{cm}\sqrt{\text{Hz}}}{\text{W}}$ while for hybrid graphene-PbS systems can reach about $1 \times 10^{13} \frac{\text{cm}\sqrt{\text{Hz}}}{\text{W}}$, similar to commercial detectors based on III-V materials.⁶⁷

Wavelength range, measured in nm. The wavelength range indicates which part of the electromagnetic spectrum can be detected, at a given NEP. The limiting factor is usually the bandgap of the active material, which determines the absorption edge. For the detectors relying on photons to generate an electron-hole pair, the absorption edge defines the longest wavelength that can be detected. Detectors working with thermal processes can overcome this limit.

4 Transition metal (Mo,W) dichalcogenides photodetectors

Transition metal dichalcogenides (TMDCs) are layered compounds with general formula MX_2 where M is a metal from group IV, V or VI of the transition metals and X is a chalcogen atom (group VI such as S, Se or Te).¹² In every layer, the metal atoms are covalently bonded to the chalcogen atoms on either side (for a schematic, see Figure 12). This covalent bond provides the structural integrity to a single layer. To form a bulk crystal, several layers are held together by weak van der Waals interaction. This weak out-of-plane interaction facilitates micro-mechanical exfoliation, allowing isolation of single layers. The mechanical exfoliation of these materials has opened the door to the fabrication of FETs based on single- and few-layer TMDCs and the study of their (opto)electronic properties. For more details on TMDCs, including their structure and their electronic properties, we refer the reader to refs.^{12,76}

4.1 Molybdenum disulphide

MoS_2 is the most studied semiconducting TMDC. Its large and direct bandgap (1.8 eV)^{15,18,20,21}, its mobility^{19,77} above $100 \text{ cm}^2 \text{ V}^{-1} \text{ s}^{-1}$ and its remarkable mechanical properties^{24,78} make single and few-layer MoS_2 an interesting material for optoelectronic and flexible devices.^{34,39,74,75,79–86}

Externally biased photodetectors. Photodetectors based on single- and few-layer MoS_2 are usually in the form of photo-FETs (see Figure 5a). Yin *et al.*⁷⁴ first reported a photo-FET based on single layer MoS_2 (Figure 5a) reaching a responsivity of about 7.5 mA W^{-1} in electron accumulation, measurable photoresponse up to about 750 nm and a response time in the order of 50 ms (see Figure 5b).⁷⁴

Recently, a similar study by Lopez-Sanchez *et al.*⁷⁵ reported a low-bound responsivity for exfoliated 1L MoS_2 photo-FET 880 A W^{-1} in depletion and a cut-off wavelength of 680 nm (see Figure 5c).⁷⁵ The reported responsivity is a lower bound since it is estimated in the OFF state of the photo-FET, where the photocurrent magnitude is the lowest.⁷⁵ With increasing power, the photocurrent raises sublinearly (Figure 5d). The time response is in the order of 4 s and it could be reduced to 600 ms with the help of a gate pulse to reset the

conductivity of the FET.⁷⁵ Both the sublinear behavior of the photocurrent with power and the need of a gate pulse to reset the conductivity are symptomatic of a photocurrent generation mechanism where trap states play a dominant role.

The NEP reached by the photodetector presented by Lopez-Sanchez *et al.* is $1.8 \times 10^{-15} \text{ WHz}^{-\frac{1}{2}}$.⁷⁵ This remarkably low NEP stems from the low magnitude of the dark current in electron depletion, achievable due to efficient field-effect tunability in single-layer MoS_2 and the 1.8 eV bandgap of 1L MoS_2 that suppresses thermally activated carriers.¹⁹

In the case of 1L MoS_2 grown by chemical vapor deposition (CVD), Zhang *et al.* reported responsivities in the order of 2200 A W^{-1} in vacuum and 780 A W^{-1} in air, highlighting the importance of the environment for both the electronic and the optoelectronic properties.⁸⁶ Given the large surface-to-volume ratio, adsorbates play a major role in the properties of layered materials.^{87–90} Charged adsorbates also reduce the photoresponse as they suppress the lifetime of trapped carriers by acting as recombination centers.⁸⁶ In a similar study on CVD grown MoS_2 , Perea-López *et al.*⁹¹ found a responsivity in the order of 1.1 mA W^{-1} , five orders of magnitude lower than in the case of Zhang *et al.*⁸⁶

There are a few likely reasons for the large difference in responsivity. At first, there is a difference in device resistance. The device measured by Zhang *et al.*⁸⁶ is subjected to a laser annealing procedure in vacuum, which reduces the device resistance. Moreover, the measurements in ref⁸⁶ are performed with a large and positive gate voltage, which brings the device in the ON state. The resulting device resistance is about 20 k Ω . For comparison, the device measured by Perea-López *et al.*⁹¹ has a resistance of about 2 G Ω (no annealing and zero gate voltage). Another important reason is the interdigitated electrode geometry of the device measured by Zhang *et al.*⁸⁶. The interdigitated device geometry grants a much (about 4 orders of magnitude) larger active area which contributes to a larger photocurrent and, therefore, a larger responsivity. Also the difference in spot size plays a role. Zhang *et al.*⁸⁶ employ a laser spot of about 1 mm diameter, which allows them to expose the whole active area of the detector. In the study of Perea-lopez *et al.*⁹¹, a 2 μm laser spot is used, limiting the illuminated area to a small portion of the device. Finally, as a consequence of the larger active area and lower resistance, Zhang *et al.*⁸⁶ are able to illuminate the device with lower optical power before hitting the noise floor of the current amplifier. Usually, at low optical powers the responsivity is the highest (see Equation 8). Therefore, the applied gate voltage, the interdigitated electrode geometry and the lower optical excitation power all contribute to the much larger responsivity reported by Zhang *et al.*⁸⁶

Both exfoliated and CVD-grown MoS_2 display large responsivity (large optical gain), sub-linear I_{photo} with incident optical power and ms-to-s response times; all these proper-

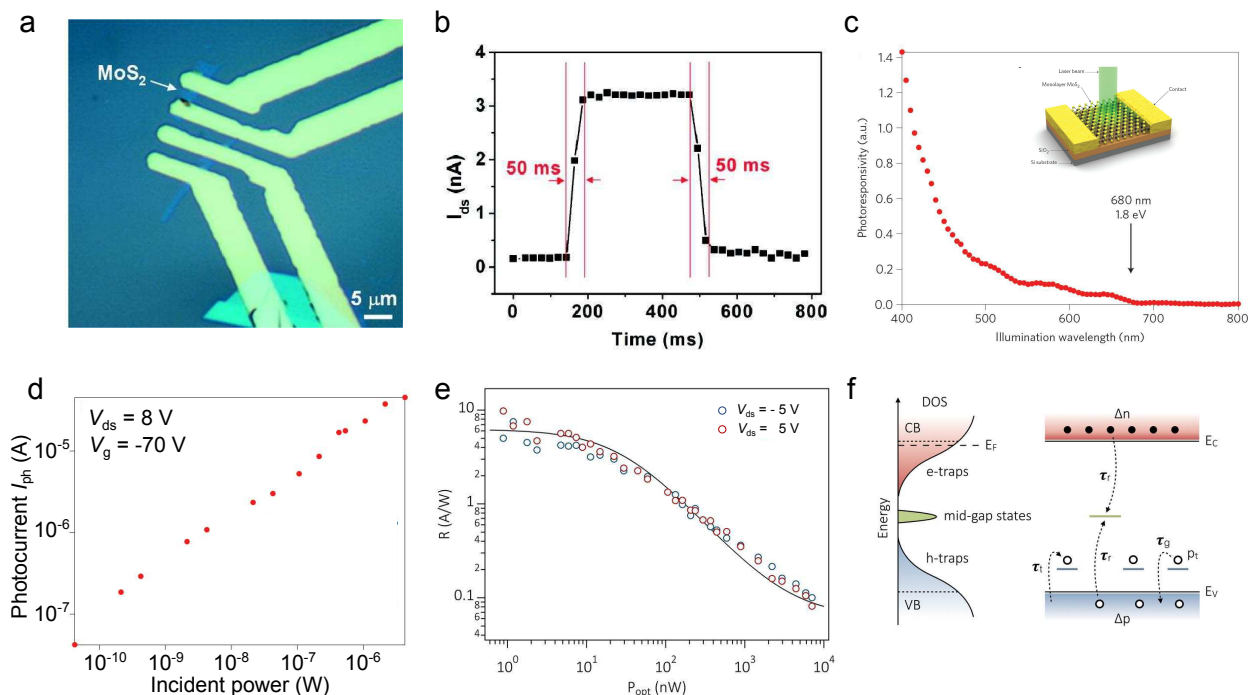


Fig. 5 (a) Optical image of a typical device based on single layer MoS₂. (b) Time response of the device in panel (a). (c) Photoresponsivity as a function of illumination wavelength, evidencing the cut-off wavelength at 680 nm. Inset: device schematics. (d) Photocurrent as a function of incident optical power. (e) Responsivity as a function of excitation power for $V_{ds} = -5$ V (blue dots) and $V_{ds} = 5$ V (red dots). Solid black line: fit with parameters from panel f. (f) Energy and relevant rates for the trap-assisted recombination model. Hole traps are the only relevant traps due to the large effective mass of the holes (open dots) compared to the electrons (closed dots). Panels a,b are adapted with permission from ref.⁷⁴ copyright 2012 American Chemical Society. Panels c,d are adapted by permission from Macmillan Publishers LTD: Nature Nanotechnology ref.⁷⁵, copyright 2013,. Panels e,f adapted with permission from ref.³⁴ copyright 2014 American Chemical Society.

ties point to a photogeneration mechanism in which trap states to the SiO₂-bound trap states and thus result in a lower optical gain. In particular, the photocurrent generation mechanism is a combination of both photoconductive (PC) technique, modulating the light excitation at a frequency faster than the PG effect. To model the acquired data (Figure 5e), *et al.*³⁴ study the photoresponse of single and bilayer MoS₂ a model based on mid-gap states and hole-trap states is proposed (Figure 5f). From this model they extract the density of modulation frequency of the optical excitation. The large difference in time scales between PC (fast) and PG (slow) facilitates disentangling the two effects.

Multilayer MoS₂ photodetectors.

Multilayer MoS₂ photodetectors benefit from the bandgap reduction, allowing for interface between the MoS₂ channel and the SiO₂ surface, extended detection range,^{81,82} larger absorption due to unlikely hydrated by water adsorbates. The surface density of increased thickness,⁸⁵ and achieve responsivity much lower than the best single-layer photodetectors. The reduction in responsivity from DC photocurrent measurements, in agreement with pre-sponsivity is possibly due to their indirect bandgap.^{34,94} The previous literature on carbon-nanotube transistors.⁹² These SiO₂-photodetection mechanism in multilayer MoS₂ is still dominated by trap states.

In conclusion, biased photodetectors based on single- and multilayer MoS₂ routinely achieve high responsivity, indicating that the slow PG is attributed to long-lived trap states at the interface between the MoS₂ channel and the SiO₂ surface. The fast PC response is attributed to both mid-gap states and hole-trap states that are caused by defects within the MoS₂. Table 4 summarizes the main figures-of-merit of this type of photodetectors.

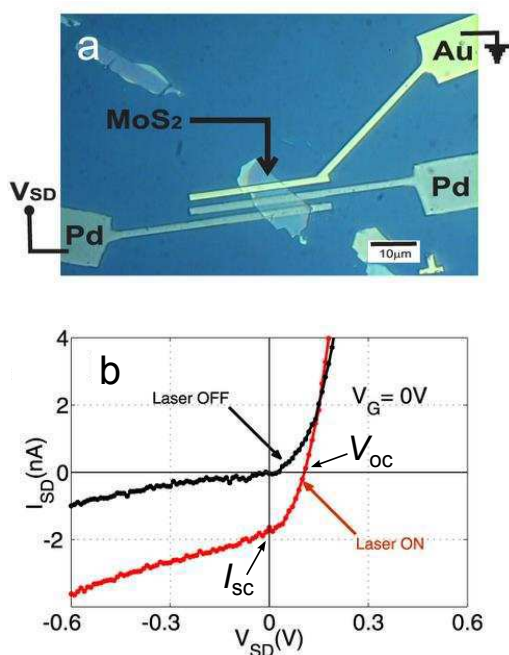


Fig. 6 (a) Optical image and circuit schematic of a typical ultrathin MoS₂ device contacted with different metals (Au and Pd). (b) $I_{ds}-V_{ds}$ characteristics of the device in panel a, in dark (solid black line) and under illumination (solid red line). Both panels are adapted by permission from Macmillan Publishers LTD: Scientific Reports ref.⁸³, copyright 2013

Photovoltaic and photo-thermoelectric effects in MoS₂. In a recent study, Fontana *et al.*⁸³ reported photovoltaic effect in a photo-FET based on a thin (~ 50 nm) MoS₂ flake where the source/drain contacts were made from gold and palladium, respectively.⁸³ The workfunction difference between Au and Pd promotes a small difference in local doping of the MoS₂ flake, giving rise to an asymmetry in the SBs at the two contacts, as in the case of graphene phototransistors.^{69,83} The SBs asymmetry effectively acts as an internal electric field and generates a photocurrent under global illumination ($r_{spot} \gg L_{device}$). An independent study on a similar device based on single-layer MoS₂ with Au and Pd contacts has demonstrated that the SB height for Pd contacts is larger than for Au.⁹⁵

Figure 6a shows a micrograph of the device by Fontana *et al.*,⁸³ highlighting the asymmetric metallization of the contacts. The measured $I_{ds}-V_{ds}$ characteristics are plotted in Figure 6b and show diode-like behavior in the dark and a clear PV photocurrent generation under illumination. For different devices, the short-circuit current I_{sc} ranges from 0.2 to 2 nA and the open-circuit voltage V_{oc} from about 30 to 100 mV. The large current in reverse bias indicates non-ideal diode behavior.

Buscema *et al.*³⁹ have performed a scanning photocurrent microscopy (SPCM) study of a single layer MoS₂ photo-FET

and found a strong and tunable photo-thermoelectric effect.³⁹ Figure 7a shows an AFM image of one of the studied devices. The contacts (Ti/Au) are deposited on top of an exfoliated MoS₂ flake on a SiO₂/Si substrate. The flake is single-layered between contacts 3 and 6. Electrode 3 is connected to a current-to-voltage amplifier while the other electrodes are grounded.

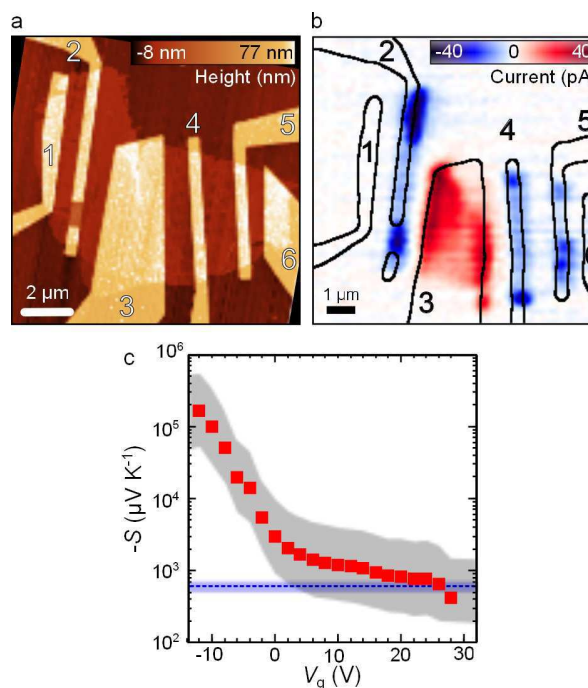


Fig. 7 (a) AFM image of one of the studied devices. Scale bar is 2 μm . (b) SPCM map. The photocurrent (linear colorscale) is collected simultaneously with the intensity of the reflected light, which is used to detect the contour of the electrodes (solid black lines). Excitation is provided by a CW laser, $\lambda = 532$ nm, $P = 1$ μW , spot radius ~ 400 nm. (c) Estimated Seebeck coefficient vs. gate voltage. The gray shaded area is the uncertainty in S due to the uncertainty in the estimation of the temperature difference. The dashed light blue line corresponds to the Seebeck coefficient value of bulk MoS₂ with experimental uncertainty (shaded light blue area). All panels are adapted with permission from ref.³⁹ copyright 2013 American Chemical Society.

With above-bandgap illumination, the SPCM measurements shown in Figure 7b reveal that the photocurrent is generated even when the laser spot is focused *on top of* the electrode area, as particularly evident for electrode 3. Measurements performed with below bandgap illumination show the same qualitative behavior, with lower photocurrent values.³⁹ The current generation inside the electrode area and its persistence with below-bandgap illumination point to a photocurrent generation mechanism dominated by the photo-thermoelectric effect, as already demonstrated for graphene also for ultra-

fast terahertz detection.^{96,97} From the sign of the photocurrent, the authors concluded that Seebeck coefficient of single-layer MoS₂ is negative, as expected for an n-type semiconductor.

The magnitude of the Seebeck coefficient S can be calculated by measuring the generated photo-thermoelectric voltage V_{PTE} and dividing it by the temperature gradient, estimated via finite element simulations. The resulting S is plotted against the gate voltage in Figure 7c. In electron accumulation, the S of single-layer MoS₂ is in agreement with its bulk value. As the channel is depleted, the Seebeck coefficient rapidly increases by two orders of magnitude, reaching $\sim 1 \times 10^5 \mu\text{V K}^{-1}$. This value is in reasonable agreement with recent electrical measurements where the temperature gradient is monitored with on-chip heaters and thermometers.⁴⁸ This large value of S and its gate tunability render single-layer MoS₂ an interesting material for applications such as thermoelectric nanodevices.

We note that, under external bias and focussed illumination, also the PV effect at the Schottky barriers (SBs) could play a role. This has, for example, been reported in multilayer MoS₂ devices which have shown photocurrent generation from SBs under external bias.⁸⁵

In conclusion, zero-bias photocurrent generation in single-layer MoS₂ is dominated by the PTE effect due to the large values of the S coefficient, while, in multilayer samples the PV effect can significantly contribute to the photocurrent.

4.2 Molybdenum diselenide

Molybdenum diselenide (MoSe₂) has been grown via CVD techniques by several groups,^{98–105} yielding large-area triangular flakes or continuous films on a variety of substrates. Photodetectors were patterned on the as-grown films or flakes were transferred to an oxidized silicon wafer to fabricate photo-FETs.

Typical CVD grown MoSe₂ photodetectors show responsivity between 0.26 mA W^{-1} (ref.⁹⁹) and 13 mA W^{-1} (ref.¹⁰⁵). Recently, a photodetector based on a $\sim 20 \text{ nm}$ thick MoSe₂ exfoliated flake, deterministically transferred on Ti electrodes, demonstrated a responsivity¹⁰⁶ up to 97.1 A W^{-1} . The response time is in the order of few tens of milliseconds for all the studied devices.

4.3 Tungsten disulfide

Tungsten disulfide (WS₂) has also been employed for photodetection.^{109,110} In their recent study, Huo *et al.*¹¹⁰ show a significant dependence of the photoresponse on the gaseous environment in which the measurements were performed.¹¹⁰ At low excitation powers, the responsivity ranges from $\sim 13 \text{ A W}^{-1}$ in vacuum to 884 A W^{-1} in a NH₃ atmosphere. The increase of responsivity in the NH₃ atmosphere was at-

tributed to charge transfer from the absorbed molecules to the WS₂ flake, which affects the WS₂ doping level, as seen in luminescence experiments.⁹⁰ As a result of the charge transfer, the lifetime of (one of the) photogenerated carriers can be extended, leading to an enhancement in the responsivity.

The relevant figures-of-merit for MoSe₂ and WS₂ photodetectors are summarized in Table 4 to facilitate a direct comparison between photodetectors based on MoS₂, MoSe₂, WS₂ and WSe₂.

4.4 Tungsten diselenide

Photodetectors. Zhang *et al.*¹¹¹ demonstrate the large impact of the metal contacts to a tungsten diselenide (WSe₂) flake on the photoresponse. The responsivity reaches 180 A W^{-1} with Pd contacts and decreases by a factor ~ 30 with Ti contacts. Conversely, the time response for the devices with Ti contacts is less than 23 ms while for the Pd contacts it is in the order of tens of seconds. The large variation in responsivity is attributed to the large difference in SBs induced by Pd and Ti, which is of general importance for photodetectors based on 2D materials.

Electrostatically defined PN junctions. In contrast to MoS₂, MoSe₂ and WS₂, devices based on WSe₂ readily demonstrate ambipolar transport via electrostatic gating.^{112–117} Exploiting this property, locally-gated PN junctions have been realized with single-layer WSe₂.^{40,107,108,118} In the following, we will review the recent studies concerning such PN junctions. We refer the reader to Table 4 for a synthetic presentation of the photodetection performance of both the photodetector of ref.¹¹¹ and the PN junctions.

The schematics of the locally-gated PN junction devices in references^{40,107,108} are presented in Figures 8a,b,c. The fabrication of these PN junctions relies on the deterministic transfer of single-layer WSe₂ on top of two local gates covered with a dielectric, which can be made from a conventional (HfO₂¹⁰⁷ or Si₃N₄¹⁰⁸) or layered (hBN)^{40,118} material. The single-layer WSe₂ is then contacted with electrodes providing low Schottky barriers, usually a Cr/Au stack.^{40,107}

The local gates allow effective control of the charge carrier type and density in the WSe₂ channel and, thus, can induce different carrier types in adjacent parts of the channel, giving rise to a PN junction. Looking at the $I_{\text{ds}}-V_{\text{ds}}$ characteristics highlights the effect of the local gates on the electrical transport, as Figures 8d,e,f illustrate. As a function of the gate configuration, the $I_{\text{ds}}-V_{\text{ds}}$ curves range from metallic (PP or NN) to rectifying with opposite direction (PN or NP).

Consistently across three independent studies, the $I_{\text{ds}}-V_{\text{ds}}$ curves in PN and NP configuration present a high resistance in parallel to the device (R_{par}) and a low saturation current (I_{sat}), both indicating nearly ideal diode behavior. This favorable behavior can be attributed to the large bandgap of single-layer

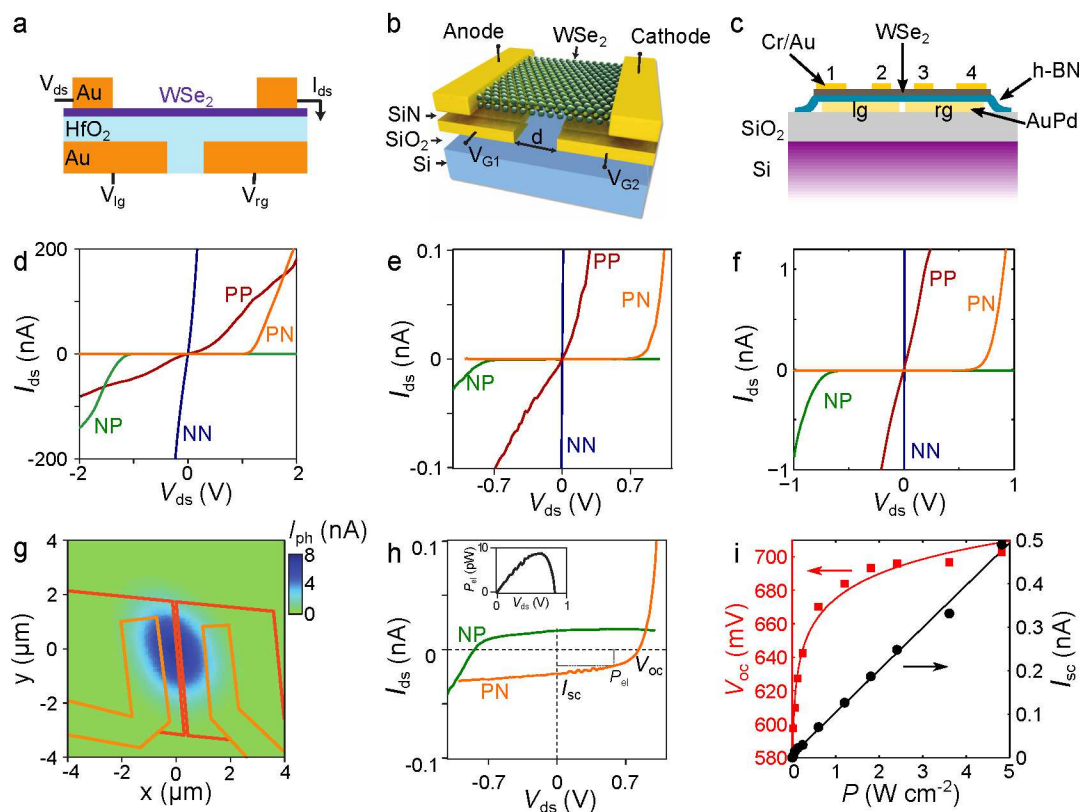


Fig. 8 (a) to (c) Device schematics: panel (a) from ref.¹⁰⁷, panel (b) from ref.¹⁰⁸ and panel (c) from ref.⁴⁰. (d) to (f) I_{ds} – V_{ds} characteristics measured in different gate configurations; (d) from ref.¹⁰⁷, (e) from ref.¹⁰⁸ and (f) from ref.⁴⁰. (g) SPCM map of the photocurrent of the device in (a) in PN configuration. (h) I_{ds} – V_{ds} characteristics measured in PN and NP configuration under white light illumination for the device in (b). Inset: electrical power (P_{el}) extracted from the device. (i) V_{oc} (left axis) and I_{sc} (right axis) as a function of excitation power for the device in (c). Panels (a), (d) and (g) are adapted by permission from Macmillan Publishers LTD: Nature Nanotechnology, reference¹⁰⁷, copyright 2014. Panel (b), (e) and (h) are adapted by permission from Macmillan Publishers LTD: Nature Nanotechnology, reference¹⁰⁸, copyright 2014. Panels (c), (f) and (i) are adapted with permission from ref.⁴⁰, copyright 2014, American Chemical Society. For the I_{ds} – V_{ds} in panels (d) to (f) the gate configurations are as follows: PP (both gates with negative bias), PN and NP (gate at opposite bias), NN (both gates at positive bias). The specific values of the gates voltages differ per device.

WSe₂ which reduces parallel pathways for current flow, such as thermally-activated carriers and field emission. The devices are also less resistive in the NN configuration than in the PP configuration. This may indicate a larger SB for hole injection resulting from the Cr/Au contacts. The difference in the absolute magnitude of I_{ds} between these studies may be attributed to differences in device fabrication, gate-induced carrier density or measurement conditions.

We now turn our attention to the response to light excitation of such locally gated PN junctions. Figure 8g shows a false-color map of the photocurrent obtained by SPCM on the device in Figure 8a in NP gate configuration.¹⁰⁷ Even though the spatial resolution is limited by the long wavelength of the excitation laser, the photocurrent peaks at the depletion region (separation between the gates), suggesting that the photocur-

rent generation is indeed dominated by the PN junction electric field.

In Figure 8h we show the I_{ds} – V_{ds} in PN and NP configuration under illumination for the device in Figure 8b. In both curves, the reverse current increases, giving rise to a short-circuit current I_{sc} and an open-circuit voltage V_{oc} . These signatures clearly indicate that the photocurrent generation is driven by the photovoltaic effect, as expected in a PN junction. The extracted electrical power is between tens of pW¹⁰⁸ and hundreds of pW (see inset of Figure 8h for a representative plot).^{40,107}

Figure 8i plots the V_{oc} (left axis) and I_{sc} (right axis) for increasing excitation power. The I_{sc} increases linearly while the V_{oc} increases logarithmically, confirming the ideal diode behavior, observed in the three independent studies.^{40,107,108} As

a zero-biased photodetector, the external quantum efficiency (EQE) can be estimated from I_{sc} and it is in the order of 0.1 ~ 0.2% at $\lambda = 532$ nm (see Figure 8f, left axis).^{40,107} The NEP of detectors based on locally gated single-layer WSe_2 is expected to be low in photovoltaic operation, due to the negligible dark current. The time response is in the order of 10 ms and reduces in reverse bias.⁴⁰

5 Ga, In and Sn chalcogenide photodetectors

Besides the previously discussed chalcogenides, also gallium – Ga – and indium – In – chalcogenide compounds are interesting for application as photodetectors.^{119–126} Similarly to the TMDCs, these layered materials are held together with van der Waals forces. However, the structure of a single layer is different from single-layered TMDCs. In compounds with 1:1 stoichiometry, like GaS, the atoms in each layer have the following repeating unit: S–Ga–Ga–S (Figure 12c). In a direction perpendicular to the layer plane, the atoms are arranged in a graphene-like honeycomb lattice.¹²² For GaS and GaSe, this crystal structure leads to a band structure with dominant indirect transitions (indirect: 2.59 eV, direct 3.05 eV for GaS; indirect: 2.11 eV, direct 2.13 eV for GaSe).^{127–131} The structure of GaTe is slightly different, leading to a dominant direct transition (1.7 eV).¹³² Compounds with different stoichiometry (like In_2Se_3) have a more complex layer structure (Figure 12c) and a variety of structural phases influencing their electrical properties. The α -phase has a direct bandgap of 1.3 eV.^{133–135} The numerical values of the bandgap are summarized in Table 2 for convenience.

Photodetectors in the form of photoFET have been realized with multilayer flakes of these materials on regular SiO_2/Si substrates and on flexible substrates (see Figure 9a), showing similar performances. GaSe and GaS^{119,122} reach responsivity of $4 A W^{-1}$ and detectivities of $2 \times 10^{14} \frac{cm\sqrt{Hz}}{W}$, in the UV-blue range (Figure 9b). On the other hand, direct bandgap materials (GaTe and In_2Se_3)^{123,136} show responsivities of about $1 \times 10^4 A W^{-1}$ at low optical excitation power (Figure 9c). The photocurrent raises sublinearly as a function of excitation power, indicating that trap states play an important role in the photoconduction mechanism.^{119,122,123,136} The time response ranges from ms to s.

A particular case is represented by InSe. It has a direct bandgap of about 1.3 eV (bulk) and reducing its thickness to below ~ 6 nm leads to a transition to an indirect bandgap of higher energy.¹²⁴ The performance of photodetectors based on 10-nm-thick InSe flakes have been studied independently by Lei *et al.*¹²⁵ and Tamalampudi *et al.*¹²⁶. In their detailed study, Lei and colleagues¹²⁵ report photocurrent spectra of 4-layer-thick InSe under excitation wavelength up to 800 nm. The tail of the photocurrent *vs.* wavelength spectra is well

fitted by a parabolic relation, strongly suggesting the indirect nature of the bandgap in ultrathin InSe. The responsivity of these devices is about $35 mA W^{-1}$ and the response time is in the order of 0.5 ms. In their study, Tamalampudi and colleagues¹²⁶ fabricate photoFETs based on ~ 12 nm thick InSe on both an oxidized Si wafer and a bendable substrate. They measure gate tunable responsivities up to about $160 A W^{-1}$ and time response in the order 4 s. Both the larger responsivity and the much longer response time compared with the study of Lei *et al.*¹²⁵ indicate that long-lived trap states enhance the photoresponse in the devices studied by Tamalampudi¹²⁶.

Very recently, also Sn chalcogenide layered compounds have been used in photodetectors applications. Specifically, SnS_2 has attracted recent attention as semiconductor material for transistors and photodetector. Exfoliated flakes have been recently employed as channel materials in FETs¹³⁷ while chemically synthesized nanoparticle films of SnS_2 have already shown promising photoresponse.¹³⁸ Su *et al.*¹³⁹ have grown flakes of SnS_2 via a seeded CVD technique and used them as channel material for photoFET. SnS_2 -based photodetectors show gate-tunable responsivity up to about $8 mA W^{-1}$ and response time of ~ 5 μs , indicating a very fast photoresponse. Table 6 summarizes the main figures-of-merit of detectors based Ga, In and Sn chalcogenides.

In conclusion, Ga, In and Sn compounds show responsivities that are comparable or larger than the one measured from TMDC based photoFETs. Moreover, their operation can be extended to the UV region of the spectrum, a feature that can enable them to be used in UV detectors. InSe shows a direct-to-indirect transition for the bandgap when its thickness is reduced below 6 nm, resulting in a parabolic absorption tail up to 1.4 eV photon energy. Thicker InSe flakes show large responsivity (about $160 A W^{-1}$) and response time in the order of few seconds, indicating a strong effect of trap states on their photoresponse. Detectors based on SnS_2 can reach responsivity of about $8 mA W^{-1}$ and fast response time, making them promising as fast detectors.

6 Ti, Hf and Zr trichalcogenides photodetectors

In the previous Section, we reviewed the state-of-art in photodetection with layered semiconducting TMDCs and Ga, In and Sn chalcogenide which demonstrate large responsivities in the visible range and have shown the possibility of realizing versatile devices through local gating. However, there are even more semiconducting chalcogenide compounds whose electronic properties in the ultra-thin limit are not yet explored.

In this Section, we review the latest literature on photodetectors based on transition metal *trichalcogenides* materials: TiS_3 ,¹⁴⁰ HfS_3 ,¹⁴¹ and ZrS_3 .¹⁴² These trichalcogenide com-

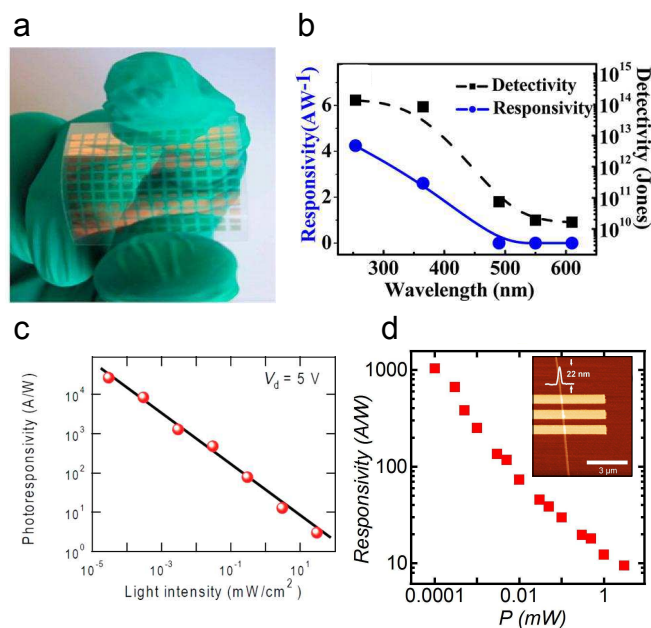


Fig. 9 (a) Photograph of flexible photodetector based on GaS flakes. (b) Responsivity (left axis) and Detectivity (right axis) of a GaS photodetector as a function of excitation wavelength. (c) Log-log plot of the responsivity as a function of excitation power for a GaTe photodetector. (d) Log-log plot of the responsivity as a function of excitation power ($\lambda = 640$ nm) for the single TiS_3 NR device shown in the inset. Panels a and b are adapted with permission from ref. ¹²², copyright 2013, American Chemical Society. Panel c is adapted with permission from ref. ¹³⁶, copyright 2013, American Chemical Society. Panel d is adapted with permission from ref ¹⁴⁰, copyright 2014, John Wiley & Sons.

pounds present a direct bandgap with energy between 1 eV and 3.1 eV. The values are reported in Table 2. Island *et al.*¹⁴⁰ have studied the photoresponse of ultrathin TiS_3 nanoribbons (NR) and achieved responsivity up to 2910 A W^{-1} at 640 nm illumination wavelength, photoresponse to wavelengths up to 940 nm and short response times (fall time ~ 5 ms). The devices were fabricated on isolated TiS_3 nanoribbons via electron-beam lithography (see inset of Figure 9d). As grown TiS_3 ribbons (100–300 nm thick, 1–10 μm wide and 10–100 μm long) were mechanically exfoliated (to a thickness down to 13 nm) and transferred to a 285 nm SiO_2/Si substrate.^{140,143} Figure 9d shows a log-log plot of the responsivity as a function of excitation power for a representative device from reference¹⁴⁰. The responsivity reaches about 1000 A W^{-1} at low power and decreases with increasing optical power. Again, the large responsivity and the decrease of the responsivity with optical power suggest that trap states play a large role in the photoreponse of ultrathin TiS_3 NR.

To obtain single HfS_3 ribbons, Xiong *et al.*¹⁴¹ dispersed

Material	Bandgap (eV)	Remarks	Ref
GaTe	1.7	direct	136
GaSe	2.11	direct at 2.13 eV	119
GaS	2.59	direct at 3.05 eV	122
In_2Se_3	1.3	direct, α -phase	123
InSe	1.3	direct	125,126
SnS_2	2.2	direct	138,139
TiS_3	1	direct	140
ZrS_3	2.56	direct	142
HfS_3	3.1	direct	144

Table 2 Bulk bandgap of Ga, In and Sn chalcogenides and Ti, Hf and Zr trichalcogenides.

part of the as-grown material in ethanol and drop-cast it onto a 300 nm SiO_2/Si substrate. Next, photolithography and metal evaporation were used to contact the randomly dispersed nanoribbons. The fabricated devices showed p-type behavior with ON currents in the order of few pA. Under illumination, the current reached up to 200 pA; the responsivity is about 110 mA W^{-1} and the time response is about 0.4 s. The measured light absorbance extends up to about 650 nm.¹⁴¹

Tao *et al.*¹⁴² studied the photoresponse of a network of ZrS_3 ribbons transferred onto flexible substrates, polypropylene and paper. Electrical devices were fabricated by shadow-mask evaporation and, under illumination, demonstrate a responsivity of about $5 \times 10^{-2} \text{ mA W}^{-1}$, a photoresponse to excitation wavelengths up to 850 nm and a time response of 13 s.¹⁴²

In summary, from the available data, we conclude that photodetectors based on a single nanoribbon of a trichalcogenide compound can achieve responsivity comparable or larger than single layer chalcogenides ($R_{\text{MoS}_2} \sim 1000 \text{ A W}^{-1}$) and faster response times ($\tau_{\text{MoS}_2} \sim 50$ ms). Table 5 summarizes the main figures of merit of photodetectors based on these materials. The large responsivity and fast response make TiS_3 a material promising for nanoscale photodetection, highlighting the need for further studies.

7 Few-layer black phosphorus

The recently re-discovered few-layer black phosphorus (bP) is an interesting material for photodetection especially due to its intermediate bandgap between graphene and TMDCs; its reduced bandgap compared to TMDCs make few-layer bP a promising candidate to extend the detection range with sizable responsivity that is achievable with 2D materials. Black phosphorus is an elemental layered compound composed of phosphorus atoms arranged in a puckered unit cell. Its bulk form has been studied in the 80's¹⁴⁵ and, electronically, it behaves as a p-type semiconductor with mobilities¹⁴⁶ in the order of

$10000\text{ cm}^2\text{ V}^{-1}\text{ s}^{-1}$ and a bandgap of about 0.35 eV . Once exfoliated to thin layers, it shows ambipolar transport^{147–154}, mobilities^{150,153} up to $1000\text{ cm}^2\text{ V}^{-1}\text{ s}^{-1}$ and absorption edge around 0.3 eV in agreement with its bulk bandgap.¹⁵⁰ The reduced symmetry of the puckered layer structure gives rise to strong anisotropy in the properties of few-layer bP, as evidenced by the anisotropic mobility and optical absorption.¹⁵⁰

Calculations predict that the bandgap of bP depends strongly on the number of layers and it should reach more than 1 eV once exfoliated down to the single layer.^{147,151,155} Black phosphorus can, thus, bridge the gap between the large-bandgap TMDCs and zero-bandgap graphene, completing the high-responsivity detection range that is achievable with 2D layered materials.

Few-layer bP photodetectors. The research effort in bP-based photodetectors has been extensive in the past year.^{65,148,149,156} Phototransistors based on ultrathin (3 nm to 8 nm thick) bP have been fabricated on SiO_2/Si substrates. In the dark, bP-based photo-FETs readily achieve ambipolar transport via back-gating with hole mobilities in the order of $100\text{ cm}^2\text{ V}^{-1}\text{ s}^{-1}$ and ON/OFF ratio $> 1 \times 10^3$.¹⁴⁸ The authors in this study¹⁴⁸ report on the performance of the bP photo-FET as a function of excitation wavelength, power and frequency. The responsivity reaches 4.8 mA W^{-1} , the photodetector wavelength range extends up to excitation wavelengths of 940 nm and the rise and fall times are 1 and 4 ms, respectively.¹⁴⁸ The readily achieved ambipolarity, the sizable responsivity across a wide wavelength range and the fast response make few-layer bP a promising material for photodetection applications up to the NIR part of the electromagnetic spectrum.

Electrostatically defined PN junction in few-layer bP. Building on the ambipolarity, Buscema and Groenendijk *et al.*¹⁴⁹ have developed a PN junction via local electrostatic gating. The devices, based on two local split gates, combine the properties of two different 2D materials: hBN as an atomically-flat and disorder-free gate dielectric and few-layer bP as an ambipolar channel material. The devices have been fabricated by exploiting the deterministic transfer method.¹⁴³ Figure 10a shows one of the fabricated devices.

Local electrostatic gating allows effective control over the type and concentration of charge carriers, enabling a versatile electrical behavior. Figure 10b plots the $I_{\text{ds}}-V_{\text{ds}}$ characteristics of the final locally-gated device in different gate configurations. With the two gates biased in the same polarity (PP or NN configuration), the device shows metallic behavior with linear $I_{\text{ds}}-V_{\text{ds}}$ curves. When the two gates are set at opposite polarities (PN or NP configuration), the $I_{\text{ds}}-V_{\text{ds}}$ curves become rectifying with the direction of the current controlled by the gate polarities.

Under increasing illumination intensity, the $I_{\text{ds}}-V_{\text{ds}}$ curves

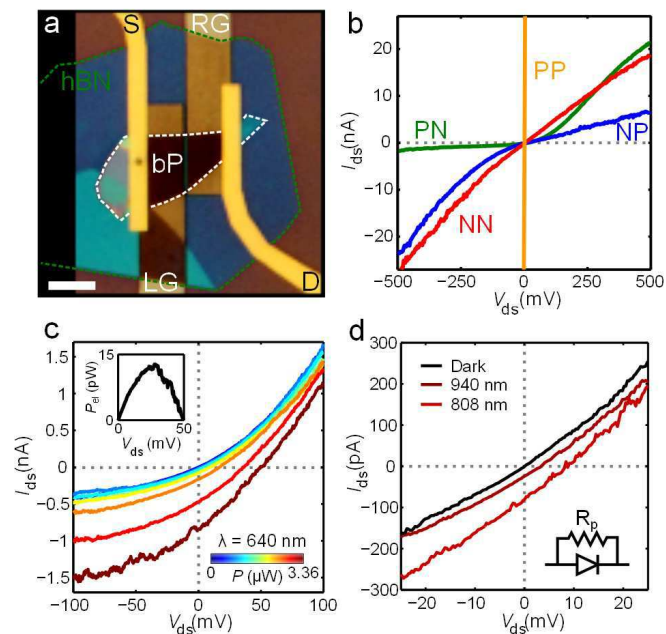


Fig. 10 (a) Optical image of one of the fabricated devices. (b) $I_{\text{ds}}-V_{\text{ds}}$ characteristics of the device in different gate configurations. (c) $I_{\text{ds}}-V_{\text{ds}}$ characteristics of the device in PN configuration under illumination with $\lambda = 640\text{ nm}$ and variable power. Inset: electric power generated by the device (d) Zoomed-in $I_{\text{ds}}-V_{\text{ds}}$ characteristics of the device in PN configuration in dark (solid black line), under illumination with $\lambda = 940\text{ nm}$ (solid dark red line) and $\lambda = 808\text{ nm}$ (solid light red line). Inset: equivalent circuit, evidencing the resistance in parallel to the junction R_p . All panels are adapted by permission from Macmillan Publishers LTD: Nature Communications, ref. ¹⁴⁹, copyright 2014.

display increasing I_{sc} and reverse current, as shown in Figure 10c. This is consistent with a photovoltaic mechanism where the generated photocurrent adds to the reverse-bias current. Thus, an extra forward bias is needed to suppress the current flow, giving rise to a non-zero V_{oc} . The inset of Figure 10c shows the electrical power ($P_{\text{el}} = V_{\text{ds}} \cdot I_{\text{ds}}$) generated by the device, which reaches about 13 pW under the largest illumination power.

Near-infrared (NIR) photons give also rise to photocurrent in the bP PN junctions. The $I_{\text{ds}}-V_{\text{ds}}$ curves in the PN configuration in the dark and with excitation wavelengths of 808 nm and 940 nm ($P_{\text{device}} = 0.33\text{ }\mu\text{W}$) are presented in Figure 10d.

Compared to PN junctions realized with WSe_2 ,^{40,107,108} bP PN junctions present a more extended wavelength operation range, comparable *EQE* but a lower V_{oc} . The lower open-circuit voltage is consistent with the smaller bandgap of few-layer bP compared to that of WSe_2 . Another limitation to the V_{oc} comes from the non-ideal diode behavior evidenced by the slope of the $I_{\text{ds}}-V_{\text{ds}}$ characteristics at $V_{\text{ds}} = 0\text{ V}$, both

in the dark and under illumination. This indicates the presence of leakage paths for the generated carriers in parallel to the junction, which can be modelled by a parallel resistance (R_p in the inset of Figure 10d). The value of R_p can be extracted by fitting the $I_{ds}-V_{ds}$ characteristics with a modified Shockley model.¹⁵⁷ For WSe_2 PN junctions, R_p exceeds $100\text{ G}\Omega$ ^{40,75,107,108} while for bP devices it is in the order of $100\text{ M}\Omega$,¹⁴⁹ evidencing the more ideal behaviour of the WSe_2 devices.

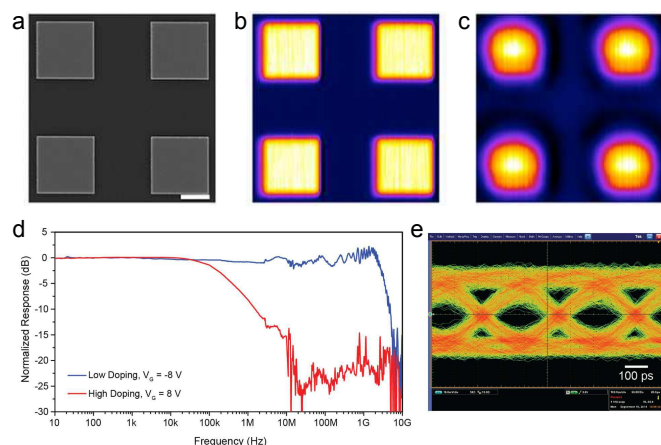


Fig. 11 (a) Scanning electron micrograph of the target image object. The scale bar is $2\ \mu\text{m}$. (b) Image of the object in (a) obtained under focused illumination with $\lambda = 532\text{ nm}$ and reading the reflected signal with a photodetector based on 120 nm thick bP. (c) Image of the object in (a) obtained under focused illumination with $\lambda = 1550\text{ nm}$ and reading the reflected signal with a photodetector based on 120 nm thick bP. (d) Photoresponse as a function of modulation frequency at low doping (blue curve) and high doping (red curve). (e) Eye-diagram for 3 Gbits/s communication. Panels (a),(b),(c) are adapted with permission from ref.⁶⁵, copyright 2014, American Chemical Society. Panels (d),(e) are adapted from ref.¹⁵⁶.

Photothermoelectric effect in few-layer bP. The thermoelectric effect plays a major role in the photocurrent generation of ultrathin bP devices. Hong *et al.*¹⁵⁸ performed scanning photocurrent microscopy (SPCM) on a 8 nm high bP transistor with a diffraction limited $\lambda = 780\text{ nm}$ laser spot as a function of polarization and gate bias. The authors find that both the PV effect (Schottky barriers) and the PTE effect contribute to the photocurrent generation.¹⁵⁸ In the OFF state, the electric field at the Schottky barriers separates the photogenerated electron-hole pairs. Applying a gate bias brings the device in the ON state and drastically reduces the contact resistance, allowing the PTE effect to contribute the photocurrent. By employing the Mott formalism (Equation 6) the authors estimate a maximum Seebeck coefficient of $\sim 100\ \mu\text{V K}^{-1}$, which is reduced by a factor 10 with increasing gate bias. Recently, the bulk Seebeck coefficient of bP was directly measured⁶¹ to be

$350\ \mu\text{V K}^{-1}$, illustrating the importance of the PTE effect in bP.

In the OFF state, where the Schottky-Barrier induced PV is dominant, the photocurrent magnitude is modulated by incident light polarization. When the polarization is aligned with the low-effective-mass crystallographic axis (x-axis) the photocurrent is enhanced; conversely, aligning the polarization with the high-effective-mass axis (y-axis) suppresses the photocurrent. The polarization-dependent photocurrent is a direct result of the strongly asymmetric band structure of few-layer bP, highlighting a difference from the isotropic TMDCS.

Imaging applications of bP photodetectors. The fast development of photodetectors based on bP has led to the realization of high performance devices for imaging^{60,65} and high-speed communication¹⁵⁶. Engel *et al.*⁶⁵ have achieved high-resolution imaging with a phototransistor based on a 120 nm thick bP flake, working via the photo-bolometric effect.^{60,65} Figure 11a shows the geometry of the objects to be imaged: $4\ \mu\text{m}$ wide metallic squares deposited on glass and separated by $2\ \mu\text{m}$. A focused laser spot is scanned over the surface of the object and the reflected signal is read by the bP phototransistor. Figure 11b,c show the images obtained by reading the electric signal from the bP photodetector at a wavelength of 532 nm and 1550 nm , respectively. The large contrast allows for clear imaging of the features. Feature visibility is constant for sizes down to $1\ \mu\text{m}$ with $\lambda = 532\text{ nm}$ and decreases by less than 20% with $\lambda = 1550\text{ nm}$.⁶⁵

High-speed applications of bP photodetectors. The study by Youngblood *et al.*¹⁵⁶ shows the photoresponse for a $\sim 11\text{ nm}$ bP flake up to GHz frequencies.¹⁵⁶ The few-layer bP is embedded in an on-chip waveguide structure with a few-layer graphene top gate, allowing for optimal interaction with light and tunability of the carrier density. The DC responsivity reaches 130 mA W^{-1} . Figure 11d shows the photoresponse of the few-layer bP device as a function of modulation frequency for low doping (blue curve) and high doping (red curve). The response rolls off at about 3 GHz for low doping and at 2 MHz for high doping. The authors ascribe this difference to a change of photocurrent generation mechanism induced by the doping.¹⁵⁶ Figure 11e shows an eye-diagram at 3 Gbits/s data rate (similar to the one reported for a graphene-based device in ref.⁶⁹). The clean eye diagram indicates that the photodetector can operate well at this high data transfer rate. This study shows that few-layer bP phototransistors, embedded in engineered devices, can achieve data transfer speed similar to graphene photodetectors^{10,11} with larger responsivities.

Table 7 summarizes the principal figures of merit of bP based detectors.

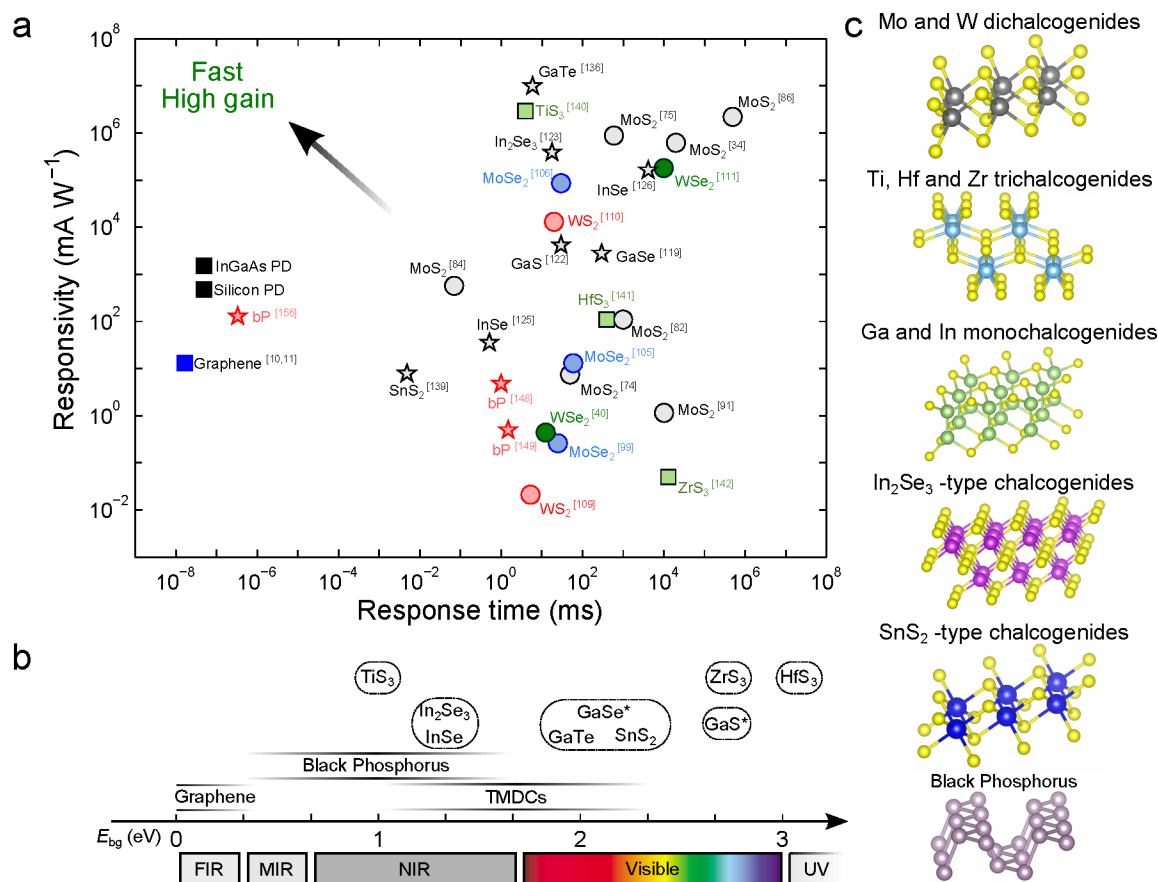


Fig. 12 (a) Responsivity against response time for the reviewed devices, for a commercial silicon and InGaAs photodiodes (black squares) and for graphene photodetectors (blue square). (b) Bandgap of the different layered semiconductors and electromagnetic spectrum. The shaded lines above and below graphene, TMDCs and black phosphorus roughly indicate the range of bandgap values that can be addressed by the various families of layered materials. The exact bandgap value would depend on the number of layers, strain level and chemical doping. The asterisk indicates that the material's fundamental bandgap is indirect. FIR: far infrared; MIR: mid infrared; NIR: near infrared; UV: ultraviolet. (c) Overview of the crystal structures of the different families of layered materials. The yellow atoms always corresponds to a chalcogen species.

8 Device comparison

In this Section, we summarize and compare the responsivity and response time of the devices we have so far reviewed. Table 4 summarizes the responsivity, rise time and spectral range for photodetectors based on MoS_2 , MoSe_2 , WS_2 and WSe_2 . Within devices based on the same material, there is a large variability in the responsivity and rise time figures-of-merit, likely indicating that the device fabrication, measurement conditions and contact metals have a large effect on the photoreponse. It is worth mentioning that, in general, most of the photodetectors based on MoS_2 present orders-of-magnitude larger responsivity and response times with respect to photodetectors based on MoSe_2 or WS_2 , possibly indicating that trap states in MoS_2 are longer-lived than in the other com-

pounds. All these compounds show a remarkable effect of the environment in which the measurements are performed, suggesting their potential application as light-sensitive gas detectors.

PN-junctions based on single-layer WSe_2 are also included in Table 4 even though their working principle is based on the photovoltaic effect, rather than photoconduction/photogating. Their responsivity is in the order of 1 to 10 mA W^{-1} when operated in the photovoltaic mode and shows a small increase in the photoconductive mode. The reported responsivity for the WSe_2 PN junctions (see Table 4) is generally lower than photodetectors based on other TMDCs, especially in comparison with MoS_2 , indicating that the internal gain mechanism (trap states) is less efficient. This is expected for photodetectors working with the photovoltaic principles. However,

locally-gated WSe₂ devices show versatile behavior, combining a photo-FET with a gate-controlled photodiode in a single device.

Table 5 summarizes the figures-of-merit for photodetectors based on and Ti, Hf and Zr trichalcogenides. Devices based on multilayers of Ga, In and Sn chalcogenides show responsivities from tens to thousands A W⁻¹ and response time between few and hundred ms. For example, GaTe photodetectors outperform detectors based on single-layer MoS₂ reaching responsivities of 1×10^4 A W⁻¹ and response time as short as 6 ms. Photodetectors based on In₂Se₃, GaSe and GaS show responsivities and response times that are slightly better than most detectors based on MoS₂. Better control over device geometry, fabrication recipes and measurement conditions are needed for a proper benchmarking, but these materials have already demonstrated their promise for visible and UV detection. Devices based on TiS₃ ultrathin nanoribbons achieve both slightly higher responsivity, faster response and wider detection range than detectors based on MoS₂. This good performance, coupled to the reduced dimensionality, make TiS₃ nanoribbons a promising material for nanostructured photodetection applications. On the other hand, both ZrS₃- and HfS₃-based detectors show poor responsivity and a slow response.

Both the semiconducting di- and tri-chalcogenides do not show photoresponse at telecommunication wavelengths. On the other hand, the newly (re)discovered black phosphorus demonstrates sizable responsivity (about 0.1 A W⁻¹) and response speed ($f_{3\text{dB}} \sim 3$ GHz) under $\lambda = 1550$ nm excitation (see Table 7). Moreover, few-layer bP has shown ambipolar transport and the possibility of realizing versatile locally-gated devices, like in the case of single-layer WSe₂. This makes few-layer bP a promising candidate for fast and broadband detection and light energy harvesting in the IR part of the spectrum. Compounds from elements in the III-VI groups (Ga, In with S, Se) are also attracting attention for photodetection applications.

To give an overview of the different materials for photodetection, the data from Tables 4 to 7 is summarized in Figure 12a. As a benchmark, the responsivity and response time of a commercial silicon photodiode (black square) and a graphene photodetector (blue square) are shown as well. It is evident that photodetectors based on semiconducting layered materials display a large (about 10 orders of magnitude) variation in their responsivity. Regarding the response time, it appears that all but one of the reviewed devices show response times larger than $\sim 1 \times 10^{-2}$ ms. The rather long response times can be attributed to the presence of long-lived trap states (in devices with responsivity above 1×10^3 mA W⁻¹) or to the limitation of the measurement electronics (RC time) likely induced by the large resistance of the device or input impedance of the current-to-voltage amplifier used in the read-out electronics.

The bP-based device presented in ref.¹⁵⁶ stands out from

the rest by showing comparable performances to both a commercial silicon photodiode and a graphene-based detector. In particular, this device shows responsivity and response times (at telecommunications wavelengths) that are within one order of magnitude from a commercial silicon photodiode (in the visible), strongly indicating that bP-based photodetectors can already compete with traditional silicon detectors.

In terms of absolute responsivity, roughly, half of the reviewed devices present values equal or larger than the Si photodiode. Especially, devices based on MoS₂, WSe₂, InSe, In₂Se₃, GaTe and TiS₃ present a responsivity which is three to four orders of magnitude above. The large responsivity supports the claim that layered semiconducting materials hold promise for ultrasensitive applications in the visible, for which the response times in the order of ms may be acceptable.

Figure 12b relates the bandgap energy of layered materials to the electromagnetic spectrum, showing that 2D semiconductors cover a very broad portion of the spectrum (from mid-infrared to the UV). We note that the exact bandgap value depends on the number of layers in a quantized fashion. To achieve continuous bandgap tunability one can employ strain engineering, chemical doping and (especially for the TMDCs) alloys of different materials, as recently proven for an alloy of MoSe₂ and MoS₂ by Li *et al.*¹⁶⁰

It also shows that there are many materials with bandgap around 1.3 eV, a region of interest for photovoltaic applications.

Figure 12c gives an overview of the crystal structures for different families of layered materials.

9 Future directions

So far, we have reviewed photodetectors that are based on a single semiconducting material, used as channel material in a photo-transistor or a locally-gated PN junction. In this Section we will discuss one of the promising directions of photodetection with semiconducting layered materials: artificial heterostructures of different layered compounds.

9.1 Artificial van der Waals heterostructures.

Deterministic transfer techniques^{13,161–165} have opened the door to the realization of artificial heterostructures based on single- or few-layer semiconducting materials. These heterostructures can be built on conventional (3D) materials (like Si^{159,166,167} and InAs¹⁶⁸) or on other two dimensional materials and have triggered a great deal of experimental work on their electrical^{23,72,169–178}, optical^{179–185} and mechanical properties.¹⁸⁶ In this Section, we review the recent experimental work aimed to establish the opto-electronic performances of devices based on these van der Waals heterostructures.

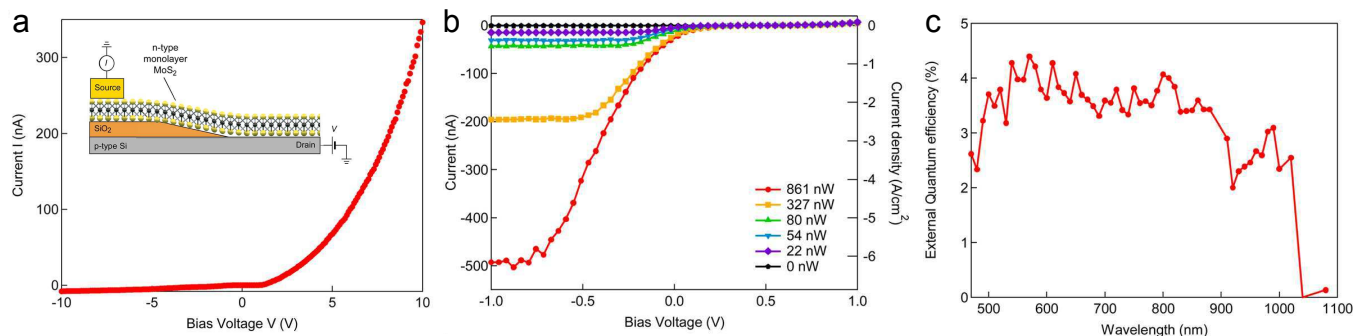


Fig. 13 (a) $I_{\text{ds}}-V_{\text{ds}}$ characteristic in the dark showing diode-like behavior. Inset: Device schematics. (b) $I_{\text{ds}}-V_{\text{ds}}$ under illumination with $\lambda = 541$ nm and varying optical power, indicated in the panel. (c) External quantum efficiency as a function of excitation wavelength. All panels are adapted from with permission from ref. ¹⁵⁹, copyright 2014, American Chemical Society.

MoS₂/Si heterostructures. A device based on single-layer MoS₂ on p-doped Si has been fabricated by Lopez-Sanchez *et al.*^{159,166} and Li *et al.*¹⁶⁷. The inset of Figure 13a shows a typical device geometry: single-layer MoS₂ is transferred on top of a highly p-doped Si substrate and charge transport occurs across the MoS₂/Si interface. In the dark, the resulting $I_{\text{ds}}-V_{\text{ds}}$ characteristics are diode-like (Figure 13a), evidencing the formation of a PN junction between the n-type MoS₂ and the p-doped Si.

Under illumination, the $I_{\text{ds}}-V_{\text{ds}}$ curves show an increased reverse-bias current and I_{sc} (Figure 13b), strongly suggesting that the photogenerated carriers are separated by the electric field generated at the interface between the single-layer MoS₂ and the Si surface. The EQE of this device reaches about 4% in the visible and decreases to about 2.5% at $\lambda = 1000$ nm (see Figure 13c).¹⁵⁹ Compared with detectors based on only single-layer MoS₂, the EQE is much lower; however, the wavelength detection range is extended due to the lower bandgap of silicon, enabling detection of NIR photons.

To conclude, devices based on MoS₂/Si heterostructures show diode-like electrical characteristics, photovoltaic effect and electroluminescence, effects that strongly indicate an efficient charge transfer at the interface between the MoS₂ and the Si substrate. Moreover, they clearly proof the possibility to integrate layered semiconductors with current silicon technology.

Graphene/TMDCs heterostructures. The inset of Figure 14a shows a schematic of a typical graphene/TMDC heterostructure; a layer of a semiconducting TMDC is covered with single-layer graphene which is contacted by metallic electrodes. In this geometry, charge is transported in the graphene layer and the TMDC serves as an additional gate dielectric with light-sensitizing properties. With this geometry, one layer of graphene over a multilayer MoS₂ re-

sulted in photodetectors with drastically enhanced responsivity ($\sim 5 \times 10^8$ A W⁻¹) at the expense of an extremely slow response times ($> 1 \times 10^3$ s).¹⁷⁰ The large responsivity stems from a strong photogating effect on the single-layer graphene channel induced by the localized states in the MoS₂ layer. Under illumination, the photogenerated holes are trapped in localized states in the MoS₂ while the photogenerated electrons are transferred to the graphene, free to circulate. The trapped holes reside longer in the MoS₂ flake and thus act as a local gate on the graphene channel. Their long lifetime is responsible for the extremely large responsivity and long response times.

Photogating has also been observed in a hybrid detector composed of a single-layer MoS₂ covered by a single layer graphene, both grown by CVD techniques.¹⁷¹ Under illumination, the $I_{\text{ds}}-V_{\text{g}}$ characteristics shift horizontally, clearly indicating that the photoresponse mechanism is dominated by the photogating effect (Figure 14a). Interestingly, the authors report a decrease of the magnitude of the photogating effect when the measurements are performed in vacuum. The smaller shift in vacuum is attributed to a reduction in the efficiency of the charge transfer between the MoS₂ and the graphene. In air, the graphene is slightly more p-type, increasing the electric field at the interface and, hence, increasing the charge transfer rate for electrons. In vacuum, the graphene is slightly more n-type, suppressing the electron transfer, thus reducing the generated photocurrent.¹⁷¹ For this device, the responsivity is also very high (about 1×10^7 A W⁻¹) at low illumination power and response times from tens to hundreds of seconds (both values for the device in air).

Graphene/TMDCs/Graphene heterostructures. In the previous Section, we have discussed two examples of graphene/TMDC heterostructures where the charge transport was measured in the graphene layer and the TMDC flake served as sensitizing material to enhance the photoresponse.

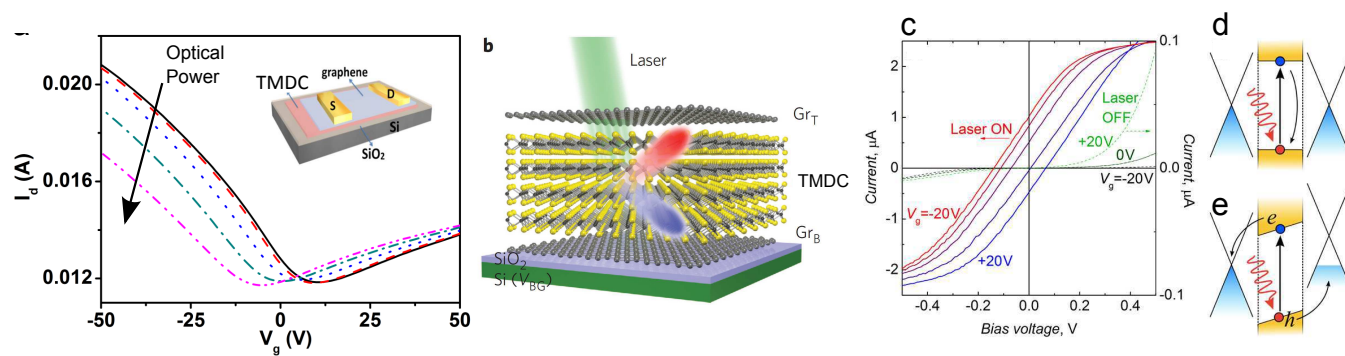


Fig. 14 (a) $I_{ds}-V_g$ characteristics for the device in panel (a) in the dark (solid black line) and under varying illumination intensities ($\lambda = 650$ nm). Inset: device schematics for graphene/TMDC heterostructures. Note that charge transport is measured across the graphene layer. (b) Device schematics for graphene/TMDC/graphene heterostructure. Note that electrical transport is measured across the two graphene layers, across the TMDC. (c) $I_{ds}-V_{ds}$ characteristics for device in panel (b) as a function of gate. The right (left) y-axis gives the current magnitude for measurements in dark, green traces (under illumination, blue to red traces). (d) Schematic band alignment in equilibrium. (e) Schematic band alignment under gate bias or chemical doping. Panels (a) is adapted by permission from Macmillan Publishers LTD: Scientific Report ref.¹⁷¹, copyright 2014. Panel (b) is adapted by permission from Macmillan Publishers LTD: Nature Nanotechnology, ref.¹⁶⁹, copyright 2013. Panels (c), (d) and (e) are adapted ref.²³ with permission from AAAS.

In this Section, we discuss devices based on vertical stacks of graphene/TMDCs/graphene where charge transport occurs through the TMDC layer in the out-of-plane direction. In other words, the graphene layers are used as transparent contacts to the photoactive TMDC layer.

In similar studies, Britnell *et al.*²³ and Yu *et al.*¹⁶⁹ fabricated vertical stacks of graphene, a ~ 50 nm thick TMDC and another graphene layer on various substrates, including SiO_2 , indium-tin-oxide (ITO) and poly-(ethylene terephthalate) (PET, a flexible and transparent polymer). Figure 14b shows a schematic of a typical device. In the dark, such devices behave as tunnel transistors in which the current can be controlled by the gate electric field (see Figure 14c, green traces).^{23,169} Under illumination, the $I_{ds}-V_{ds}$ characteristics become linear (until saturation) and show a gate-tunable I_{sc} indicating that the photovoltaic effect dominates the photocurrent generation (see Figure 14c, blue to red traces).^{23,169}

The emergence of the photovoltaic effect can be understood by looking at the band diagram schematics presented in Figure 14d and Figure 14e. In an ideal case (Figure 14d) the band alignment between the graphene layers and the TMDC is symmetric. This symmetric alignment gives no preferential direction for the separation of the photogenerated electron-hole pairs, therefore leading to zero net photocurrent. On the other hand, a small difference in the doping level of the two graphene electrodes (induced by gating or chemical doping) will result a misalignment between the bands and, thus, in a built-in electric field. This built-in electric field separates the e-h pairs and generates the I_{sc} (see Figure 14e). As a consequence, the sign and magnitude of I_{sc} are gate-tunable, as evidenced from the blue-to-red traces in Figure 14c. In both

studies, SPCM measurements reveal that the photocurrent is generated only in the regions of the heterostructure where such an asymmetry is realized.

The responsivity of these devices is in the order of 0.2 A W^{-1} and the maximum electrical power that can be generated is in the order of a few μW , much larger than current PN junctions based on single-layer WSe_2 ^{40,107,108}, making this type of devices very promising candidates for flexible solar cells.

bP/TMDC heterostructures. Also heterostructures comprising few-layer bP (p-type) and single layer MoS_2 (n-type) have recently shown gate-tunable photovoltaic effect, generating about 2 nW of electrical power.¹⁷⁷

TMDC/TMDC heterostructures. Very recently, heterostructures based on single-layered semiconducting TMDCs have also been studied. For example, heterostructures of single-layer MoS_2 and single-layer WSe_2 have been fabricated by several groups.^{72,172-174} Figure 15a shows an example of such a heterostructure from the Columbia group.¹⁷³ The WSe_2 and MoS_2 single layers have been chosen because of their natural tendency to display p- and n-type conduction, respectively. In Figure 15a, single-layer MoS_2 and single-layer WSe_2 are crossed on top of each other and are contacted with Al and Pd to enhance the n-type and p-type character, respectively

In dark, $\text{WSe}_2/\text{MoS}_2$ heterostructures show gate-tunable rectifying behavior.^{72,173} Under illumination, these heterostructures show a gate-dependent photovoltaic effect as evidenced by the $I_{ds}-V_{ds}$ characteristics in Figure 15b. The I_{sc} and V_{oc} reach a maximum at $V_g = 0$ V, the position at which the rectifying ratio is the highest.^{72,173} The inset of Figure 15b

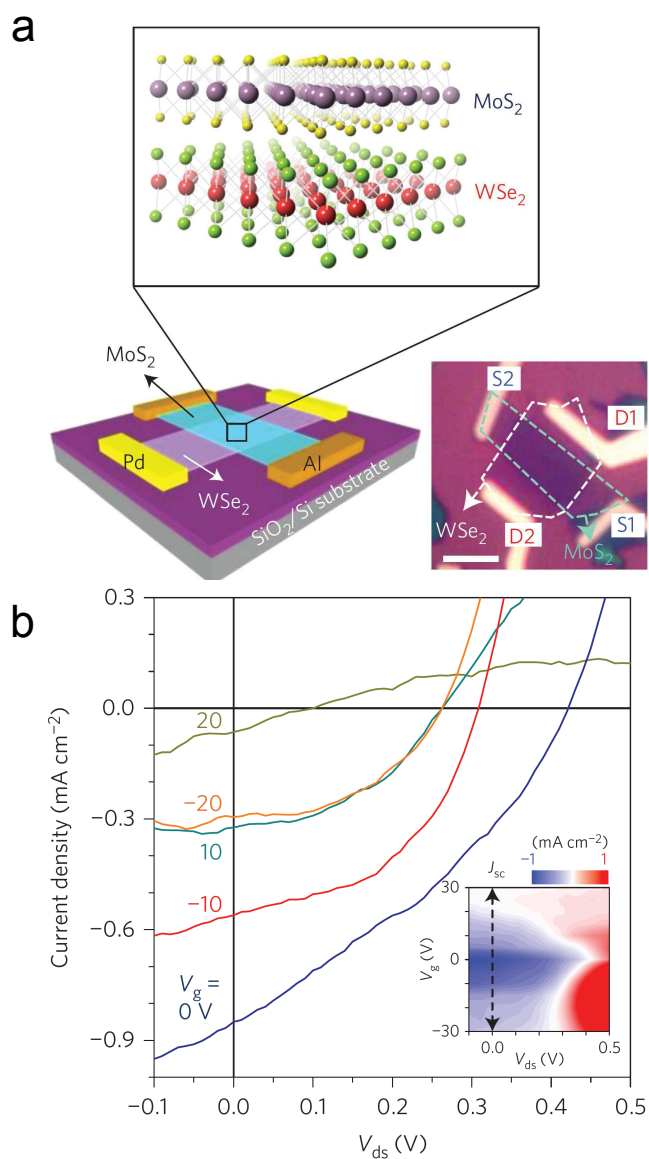


Fig. 15 (a) Device schematic. Top: schematic representation of the single layers composing the heterostructure. Left: schematic of the contact geometry. Pd (Al) is used to contact the single-layer WSe₂ (MoS₂). Right: optical micrograph of the final device. D1 and D2 (S1 and S2) indicate the contacts to the WSe₂ (MoS₂). The scale bar is 2 μm . (b) $I_{\text{ds}}-V_{\text{ds}}$ characteristics under illumination at different gate voltages. Inset: false color map of the current under illumination as a function of V_{ds} and V_{g} . Panels (a) and (b) are adapted by permission from Macmillan Publishers LTD: Nature Nanotechnology, from ref. ¹⁷³, copyright 2014.

shows a colormap of the measured current as a function of V_{g} and V_{ds} , highlighting the reduction of I_{sc} as the magnitude of the gate voltage increases. Through spatial photocurrent and photoluminescence maps the authors ascribe the origin of this

photovoltaic effect to charge transfer between the WSe₂ and MoS₂.^{72,173,174}

Huo *et al.*¹⁷⁵ have recently fabricated heterostructures based on multilayer MoS₂ and WS₂ and measured the same qualitative behavior.¹⁷⁵ CVD techniques have also been used to grow both vertical and lateral heterostructures.¹⁷⁶ CVD-grown devices showed stronger interlayer interaction compared with their transferred counterparts,¹⁷⁶ likely being caused by an improved charge transfer. An increase in the charge-transfer efficiency in CVD-grown MoS₂/WSe₂ heterostructure will likely lead to a larger rectification and stronger photovoltaic effect. In conclusion, TMDC/TMDC heterostructures present gate-tunable and strong photovoltaic power generation ($\sim 6 \mu\text{W}$) coupled to the possibility of direct CVD growth; these properties make them hold promise for large-area flexible and transparent solar cells.

CVD techniques. In recent years, there has been an intense effort in studying the CVD growth of layered compounds, especially graphene, hexagonal boron nitride and transition metal dichalcogenides. CVD growth of the semiconducting TMDCs has proven to be a reliable technique that delivers high quality large-area single layers as shown in ref.¹⁸⁷. Van der Zande's seminal work demonstrates that, with a straightforward recipe, it is possible to obtain isolated triangular single-layer MoS₂ flakes with edges length in the order of 100 μm at the side of a continuous single-layer film. The quality of the as-grown single layers is proven via luminescence and transmission electron microscopy. The other Mo- and W- based dichalcogenides can also be grown via CVD techniques – See refs.^{101,188–191}. For more extensive details on the CVD growth of single-layers of TMDCs and other layered semiconductors we refer the reader to very recent in-depth reviews.^{192,193}. The tables presented in ref.¹⁹² give a comprehensive and clear overview of the growth conditions and properties of the resulting material.

These high quality CVD-grown single layers are then used to fabricate large-area heterostructures via deterministic transfer methods. Figure 16a shows such a vertical heterostructure composed by CVD grown MoS₂ and WSe₂ single layers built on sapphire. The overlap area between the flakes is several square microns large.¹⁹⁴ These heterostructures have been mostly employed in luminescence/Raman studies,^{183,194,195} second harmonic generation studies¹⁹⁶ and mechanical studies.¹⁸⁶

More recently, the CVD growth technique has been used for direct growth of heterostructures.¹⁷⁶ These *epitaxially* grown heterostructures include TMDC-on-TMDC,^{176,182} MoS₂-on-hBN,¹⁹⁷ TMDC-on-graphene,¹⁹⁸ and MoS₂-on-SnS₂.¹⁹⁹ Figure 16b shows an example of an epitaxially grown heterostructure. The outer triangular shape is single-layer MoS₂ while the inner triangle is WS₂.¹⁸² These CVD grown heterostructures

typically assemble as concentric triangles.

Moreover, Gong *et al.* have shown the possibility to grow lateral (in-plane) heterojunctions of different materials by changing the precursors in the reactor chamber.¹⁷⁶ As shown by Yu *et al.*¹⁸², heterostructures built with transfer mechanisms show a reduced charge transfer compared to epitaxially grown ones; the charge transfer is equal after annealing the transferred heterostructures. To conclude, CVD techniques provide a reliable way to grow and fabricate heterostructures of layered semiconductors.

9.2 Surface decoration

Surface decoration is a viable way to exploit the large surface-to-volume ratio to tune the properties of layered semiconductors. In the following paragraph we will discuss surface decoration with colloidal quantum dots. In the next section, which deals with light-matter interaction enhancement, we will also discuss decoration with gold nano structures for plasmonics.

Hybrid MoS₂/Quantum-dot photodetectors. Very recently, Kufer *et al.*²⁰⁰ have realized hybrid photodetectors based on bilayer MoS₂ and lead sulfide (PbS) quantum dots. The final device was fabricated in two steps; first the bilayer MoS₂ was patterned into an FET and, second, the PbS quantum dots were deposited on top via a layer-by-layer and ligand exchange process. The ligand exchange step is crucial to improve the charge transport properties of the quantum dot film and the charge transfer to the MoS₂ bilayer. The deposition of the QDs affects the $I_{ds}-V_g$ characteristics of the bilayer MoS₂, reducing the ON/OFF ratio and mobility. This is a strong indication that the QD deposition increases the charge carrier concentration in the MoS₂ flake by charge transfer.

This hybrid photodetector shows high responsivity ($6 \times 10^5 \text{ A W}^{-1}$), detection up to $\lambda = 1200 \text{ nm}$ (Figure 16c) and a time response in the order of 350 ms. Moreover, by tuning the MoS₂ in the OFF state, the dark current can be suppressed, decreasing the NEP and increasing the detectivity of the detector. The low dark current and large detectivity are a major improvement with respect to a similar hybrid device based on single-layer graphene, where the large dark current of the graphene FETs reduces the detectivity.⁶⁷

The photodetection mechanisms are a combination of photovoltaic and photo-gating. The electric field at the interface between the n-type MoS₂ and the p-type PbS quantum dot film separates the electron hole pairs that are generated by photon absorption in either of the two materials (photovoltaic). Next, the holes are trapped in the quantum dot film, increasing the photocarrier lifetime and yielding the large responsivity and long response time (photogating).

9.3 Enhancing light-matter interaction

Several techniques can be used to further increase light matter interaction in semiconductor devices. The topic of light matter interaction enhancement has been discussed in a recent perspective paper.²⁰¹ In this Section, we only highlight two techniques that are relevant for 2D layered materials.

Plasmonic nanostructures. To further boost the photoreponse, plasmonic surface decoration has been recently incorporated in detectors based on layered semiconductors.^{23,202,203} Plasmonic structures enhance and focus the electric field of the optical excitation in a very small volume, effectively increasing the absorption cross section of the device. This enhancement has a very large effect on the device photoresponse, as can be seen in ref.²³ where the responsivity increases by an order of magnitude once the device is decorated with gold nanoparticles.

Another example of plasmonic nanostructures is presented by an ordered array of metallic objects with dimension and pitch in the order of the excitation wavelength. Figure 16d and 16e show a schematic and an optical micrograph of such a structure consisting of a 2D square lattice of 100-by-1000 nm gold nanoantennas covered by a single-layer MoS₂.²⁰⁴ The asymmetry in the dimensions of the nanoantenna makes them sensitive to the polarization of the incoming excitation (or output emission). The pitch between the nanoantennae effects the center resonance wavelength of the plasmonic structure. Such structures can be relatively easily integrated onto photodetectors based on 2D semiconductors to increase their responsivity at a certain wavelength range. Conversely, they can also be applied to LEDs to increase their emission intensity.

Photodetectors integrated onto waveguides. Waveguides are planar structures that can guide an electric field in an analogue way to optical fibers, but confined in a plane. In silicon technology, they are being studied for on-chip optical interconnects at telecommunication wavelengths ($\lambda \sim 1550 \text{ nm}$) where Si is transparent. At the boundaries of a waveguide, an evanescent field exists. By placing a thin flake of a layered semiconductor on top of a waveguide, this evanescent field can be absorbed by the material and give rise to electron-hole pairs useful for photodetection. Moreover, the interaction with the excitation electric field happens along the in-plane direction, drastically increasing the absorption cross section.

This concept has been used for graphene-based detectors, which achieved higher responsivities and large data-transfer rates.^{205–207} To the best of our knowledge, the only other layered material that has been integrated on such a structure is black phosphorus in a research work by Youngblood *et al.*¹⁵⁶ that we have highlighted in a previous section.

Optical microcavities. Other layered semiconductors (and especially the TMDCs) would not benefit from integration

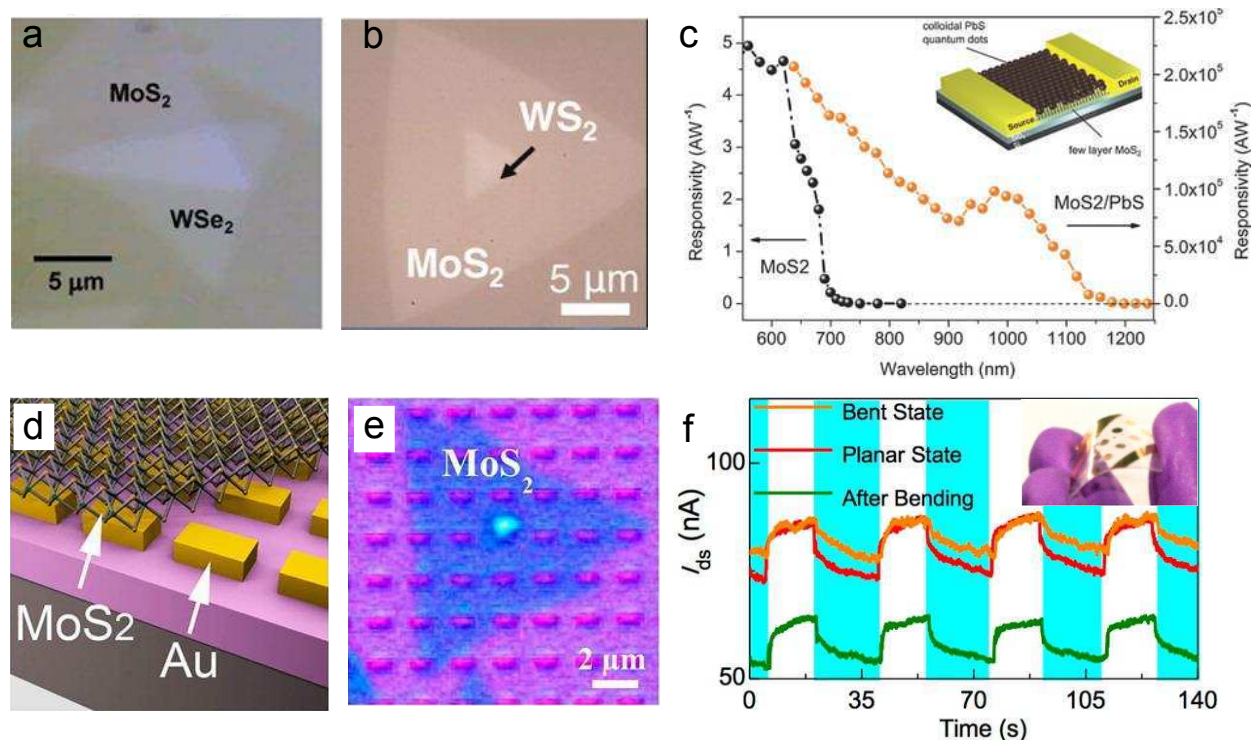


Fig. 16 (a) Optical micrograph of an artificial heterostructure built by vertically stacking single-layer MoS₂ and WSe₂ on sapphire. (b) Optical micrograph of epitaxially grown MoS₂/WS₂ heterostructure. (c) Responsivity of a few-layer MoS₂ phototransistor (black dots, left axis) and of the same transistor after decoration with PbS quantum dots (orange dots, right axis). Schematic (d) and optical micrograph (e) of a single layer MoS₂ deposited over a 2D array of gold nanoantennae. (f) Time trace of the source drain current of a flexible photodetector based on InSe. The blue shading indicates that the optical excitation is OFF. The solid red line is the time-trace in the pristine state. The orange line is recorded while the device is bent. The green solid line is recorded after one bending cycle when the device is again flat. Panel a is adapted with permission from ref.¹⁹⁴, copyright 2014, American Chemical Society. Panel b is adapted with permission from ref.¹⁸², copyright 2015 American Chemical Society. Panel c is adapted with permission from ref.²⁰⁰, copyright 2014, John Wiley & Sons. Panels d, e are adapted with permission from ref.²⁰⁴, copyright 2014, American Chemical Society. Panel f and inset are adapted with permission from ref.¹²⁶, copyright 2014, American Chemical Society.

onto silicon waveguides due to their negligible absorption at telecommunication wavelengths. On the other hand, integration within optical microcavities in the visible greatly enhances light-matter interaction in such thin crystals. Very recently, a few groups have coupled MoS₂,²⁰⁸ WSe₂,^{209,210} and GaSe²¹¹ to optical cavities to study the luminescence and demonstrate nanoscale optically-pumped lasing with very low threshold. Integration of a photodetector within an optical cavity would result in an increased responsivity at the cavity resonant wavelength, of interest for applications that require detection of a specific wavelength.

9.4 Suspended devices

Studying devices based on suspended flakes of 2D semiconductors would allow the intrinsic properties of the semiconductor to be distinguished from spurious substrate-induced ef-

fects, such as optical interference, charge or phonon scattering. In a recent work, Klots *et al.*²¹² perform photocurrent spectroscopy on suspended MoS₂, MoSe₂ and WSe₂ devices. The photocurrent spectra they acquire allow the identification of the excitonic resonances that are responsible for photocurrent generation and extract their binding energy. To the best of our knowledge, this is the only study on the photocurrent of suspended devices. This is an interesting future direction for gaining a deeper fundamental understanding of the photoconduction processes. On the other hand, the difficulty arising in suspending the devices may be limiting the current experimental effort. We speculate that employing hBN as a gate dielectric would result in a suppression of impurity scattering and surface phonons (with respect to the common SiO₂) and, by carefully choosing the thickness, will also eliminate optical interference effects. Therefore, using h-BN as substrate may yield the same fundamental understanding as suspended

devices.

9.5 Flexible electronics

Flexible (nano)electronics is an emerging applied research field motivated by the need for bendable/foldable, transparent and functional electronic devices. Layered materials hold great promise to advance this field due to their atomic thickness, high crystalline quality (yielding high mobility), transparency (and yet strong light-matter interaction) and large breaking strength (allowing for large deformations). Another advantage of layered materials lays in the possibility of growing large-area of high crystalline quality material via chemical vapour deposition (CVD) techniques, as described earlier. A recent review highlights the impact of layered materials on the perspectives of flexible electronics.²¹³

Semiconducting layered materials could offer the basis for flexible transistors²¹⁴ or flexible tunneling transistors for digital computation²¹⁵ and also the light-absorbing material for flexible photodetectors.^{122,126,216–219}

Devices are typically built by transferring a flake of a layered semiconductor onto a flexible and transparent substrate, usually a polymer (a recent review on thin-film-based flexible electronics gives an overview of the available substrates²²⁰). Electrical contacts are already present on the substrate or they are patterned afterwards lithographically. An example of a bent device is shown in the inset of Figure 16f.¹²⁶

The performances of such detectors are less than an order of magnitude lower than their analogues on rigid SiO₂/Si substrates. An interesting case is represented by a flexible photodetector based on few-layer GaS,¹²² as its performance is higher than the device built on SiO₂/Si, stressing again the strong effect of the environment on 2D materials. These devices show some signs of degradation after bending cycles.

Figure 16f shows measurements of the photoresponse of an In₂Se₃-based flexible photodetector under modulated light excitation from ref.¹²⁶. The traces acquired in the pristine state and in the bent state are very similar, indicating that bending does not affect the photoresponse. The green solid trace in Figure 16f is acquired once the bending stress is released and shows a very similar photocurrent and a lower OFF current. The similar photocurrent is again an indication that bending does not affect the photoresponse of In₂Se₃. On the other hand, the reduced OFF current is likely an indication of an increased contact resistance due to the bending, most likely induced by degradation of the contact metals.

Very recently, a flexible FET based on few-layer bP on metalized polyimide has shown unaltered electrical performances after 5000 bending cycles;²¹⁴ this is a promising indication that long-term stability to bending can be achieved. A further development would be to integrate flexible and transparent substrates with ionic polymer gating to combine the flexi-

bility and transparency with an efficient field effect tunability.

To conclude, we would like to point out that not only photodetectors, but recently also LEDs have been realized on flexible and transparent substrates.²²¹ These impressive devices have been realized by employing only 2D materials: hBN as insulator and tunnel barrier, WS₂ and MoS₂ as semiconducting layers.

10 Summary and outlook

We have reviewed the current state-of-the-art in photodetection with layered semiconducting materials. Photodetectors based on TMDCs, especially MoS₂, show large responsivity coupled to slow response times, indicating that these materials can be suitable for sensitive applications in the visible and when time response is not important. MoS₂ also possesses a large Seebeck coefficient, making it a promising material for thermal energy harvesting. Novel materials, such as tri-chalcogenides (TiS₃) nanoribbons, III-VI and IV-VI compounds (e.g. GaTe or SnS₂), show both large responsivities (larger than MoS₂ photodetectors) and fast response times, making them promising candidates for fast and sensitive photodetection applications. Few-layer black phosphorus and single-layer WSe₂ show ambipolar transport and have been employed in the realization of electrical devices that can be controlled via local electrostatic gating. Black phosphorus has shown sizable and very fast photoresponse at telecommunication wavelengths with orders-of-magnitude larger responsivity of graphene and comparable response speed, making it an interesting material for optical communications and energy harvesting.

A future direction is represented by the possibility of stacking different 2D materials to form artificial heterostructures, allowing to tailor the resulting opto-electronic properties for a specific application. This has led to ultra-high responsive photodetectors (albeit very slow) based on graphene/MoS₂ vertical stacks. Moreover, heterostructures of different TMDCs and/or graphene show great potential for solar energy harvesting in flexible and transparent solar cells. At this stage, a deeper understanding of the photocurrent and carrier recombination mechanisms is needed for optimization of device performance and large-area growth and transfer techniques will be fundamental for the realization of applications.

From an application perspective, the sizable variation in the figures-of-merit reported by different studies on the same material is an indication that device fabrication, contact metals and measurement environment play an important role in the photodetector performance. Furthermore, the fabrication process of these devices extensively relies on mechanical exfoliation. Both issues may be tackled by using CVD-grown materials, that provide large-area, uniform samples. Integration with current CMOS technology is also an important challenge.

Especially the work from Lopez-Sanchez *et al.*^{159,166} demonstrates that coupling MoS₂ to silicon can be highly beneficial. Again, CVD growth may help in integrating MoS₂ and other TMDCs in CMOS fabrication.

11 Acknowledgement

This work was supported by the Dutch organization for Fundamental Research on Matter (FOM). A.C-G. acknowledges financial support through the FP7-Marie Curie Project PIEF-GA-2011-300802 ('STRENGTHNANO').

References

- 1 L. Menon, H. Yang, S. J. Cho, S. Mikae, Z. Ma and W. Zhou, *Photonics Journal, IEEE*, 2015, **7**, 1–6.
- 2 E. Mulazimoglu, S. Coskun, M. Gunoven, B. Butun, E. Ozbay, R. Turan and H. E. Unalan, *Applied Physics Letters*, 2013, **103**, 083114.
- 3 L. Tao, E. Cinquanta, D. Chiappe, C. Grazianetti, M. Fanciulli, M. Dubey, A. Molle and D. Akinwande, *Nat Nano*, 2015, **10**, 227–231.
- 4 K. S. Novoselov, A. K. Geim, S. V. Morozov, D. Jiang, Y. Zhang, S. V. Dubonos, I. V. Grigorieva and A. A. Firsov, *Science*, 2004, **306**, 666–669.
- 5 K. S. Novoselov, A. K. Geim, S. V. Morozov, D. Jiang, M. I. Katsnelson, I. V. Grigorieva, S. V. Dubonos and A. A. Firsov, *Nature*, 2005, **438**, 197–200.
- 6 K. S. Novoselov, D. Jiang, F. Schedin, T. J. Booth, V. V. Khotkevich, S. V. Morozov and A. K. Geim, *Proceedings of the National Academy of Sciences of the United States of America*, 2005, **102**, 10451–10453.
- 7 K. S. Novoselov, E. McCann, S. V. Morozov, V. I. Fal'ko, M. I. Katsnelson, U. Zeitler, D. Jiang, F. Schedin and A. K. Geim, *Nat Phys*, 2006, **2**, 177–180.
- 8 K. S. Novoselov, Z. Jiang, Y. Zhang, S. V. Morozov, H. L. Stormer, U. Zeitler, J. C. Maan, G. S. Boebinger, P. Kim and A. K. Geim, *Science*, 2007, **315**, 1379.
- 9 C. Lee, X. Wei, J. W. Kysar and J. Hone, *Science*, 2008, **321**, 385–388.
- 10 F. Xia, T. Mueller, Y.-m. Lin, A. Valdes-Garcia and P. Avouris, *Nat Nano*, 2009, **4**, 839–843.
- 11 T. Mueller, F. Xia and P. Avouris, *Nature Photonics*, 2010, **4**, 297–301.
- 12 Q. H. Wang, K. Kalantar-Zadeh, A. Kis, J. N. Coleman and M. S. Strano, *Nat Nano*, 2012, **7**, 699–712.
- 13 L. Wang, I. Meric, P. Y. Huang, Q. Gao, Y. Gao, H. Tran, T. Taniguchi, K. Watanabe, L. M. Campos, D. A. Muller, J. Guo, P. Kim, J. Hone, K. L. Shepard and C. R. Dean, *Science*, 2013, **342**, 614–617.
- 14 J. N. Coleman, M. Lotya, A. O'Neill, S. D. Bergin, P. J. King, U. Khan, K. Young, A. Gaucher, S. De, R. J. Smith, I. V. Shvets, S. K. Arora, G. Stanton, H.-Y. Kim, K. Lee, G. T. Kim, G. S. Duesberg, T. Hallam, J. J. Boland, J. J. Wang, J. F. Donegan, J. C. Grunlan, G. Moriarty, A. Shmeliov, R. J. Nicholls, J. M. Perkins, E. M. Grieverson, K. Theuvsen, D. W. McComb, P. D. Nellist and V. Nicolosi, *Science*, 2011, **331**, 568–571.
- 15 K. F. Mak, C. Lee, J. Hone, J. Shan and T. F. Heinz, *Phys. Rev. Lett.*, 2010, **105**, 136805.
- 16 K. F. Mak, K. He, J. Shan and T. F. Heinz, *Nat Nano*, 2012, **7**, 494–498.
- 17 K. F. Mak, K. He, C. Lee, G. H. Lee, J. Hone, T. F. Heinz and J. Shan, *Nat. Mater.*, 2013, **12**, 207–211.
- 18 A. Ayari, E. Cobas, O. Ogundadegbe and M. S. Fuhrer, *J. Appl. Phys.*, 2007, **101**, 014507–5.
- 19 B. Radisavljevic, A. Radenovic, J. Brivio, V. Giacometti and A. Kis, *Nature Nanotechnology*, 2011, **6**, 147–150.
- 20 A. Splendiani, L. Sun, Y. Zhang, T. Li, J. Kim, C.-Y. Chim, G. Galli and F. Wang, *Nano Letters*, 2010, **10**, 1271–1275.
- 21 G. Eda, H. Yamaguchi, D. Voiry, T. Fujita, M. Chen and M. Chhowalla, *Nano Lett.*, 2011, **11**, 5111–5116.
- 22 W. S. Yun, S. W. Han, S. C. Hong, I. G. Kim and J. D. Lee, *Phys. Rev. B*, 2012, **85**, 033305.
- 23 L. Britnell, R. M. Ribeiro, A. Eckmann, R. Jalil, B. D. Belle, A. Mishchenko, Y.-J. Kim, R. V. Gorbachev, T. Georgiou, S. V. Morozov, A. N. Grigorenko, A. K. Geim, C. Casiraghi, A. H. C. Neto and K. S. Novoselov, *Science*, 2013, **340**, 1311–1314.
- 24 A. Castellanos-Gomez, M. Poot, G. A. Steele, H. S. J. van der Zant, N. Agrat and G. Rubio-Bollinger, *Adv. Mater.*, 2012, **24**, 772–775.
- 25 K. He, C. Poole, K. F. Mak and J. Shan, *Nano Lett.*, 2013, **13**, 2931–2936.
- 26 H. J. Conley, B. Wang, J. I. Ziegler, R. F. Haglund, S. T. Pantelides and

- K. I. Bolotin, *Nano Lett.*, 2013, **13**, 3626–3630.
- 27 C. R. Zhu, G. Wang, B. L. Liu, X. Marie, X. F. Qiao, X. Zhang, X. X. Wu, H. Fan, P. H. Tan, T. Amand and B. Urbaszek, *Phys. Rev. B*, 2013, **88**, 121301.
- 28 J. Feng, X. Qian, C.-W. Huang and J. Li, *Nat Photon.*, 2012, **6**, 866–872.
- 29 A. Castellanos-Gomez, R. Roldán, E. Cappelluti, M. Buscema, F. Guinea, H. S. van der Zant and G. A. Steele, *Nano Lett.*, 2013, **13**, 5361–5366.
- 30 A. Rose, *Concepts in photoconductivity and allied problems*, Interscience Publishers, 1963.
- 31 R. Bube, *Photoelectronic Properties of Semiconductors*, Cambridge University Press, 1992.
- 32 B. Saleh and M. Teich, *Fundamentals of photonics*, Wiley, 1991.
- 33 G. Konstantatos and E. H. Sargent, *Nature nanotechnology*, 2010, **5**, 391–400.
- 34 M. M. Furchi, D. K. Polyushkin, A. Pospischil and T. Mueller, *Nano Lett.*, 2014, **14**, 6165–6170.
- 35 S. M. Sze and K. K. Ng, *Physics of semiconductor devices*, John Wiley & Sons, 2006.
- 36 F. H. L. Koppens, T. Mueller, P. Avouris, A. C. Ferrari, M. S. Vitiello and M. Polini, *Nat Nano*, 2014, **9**, 780–793.
- 37 N. Ashcroft and N. Mermin, *Solid state physics*, Saunders College, 1976.
- 38 J. Park, Y. H. Ahn and C. Ruiz-Vargas, *Nano Lett.*, 2009, **9**, 1742–1746.
- 39 M. Buscema, M. Barkelid, V. Zwiller, H. S. J. van der Zant, G. A. Steele and A. Castellanos-Gomez, *Nano Lett.*, 2013, **13**, 358–363.
- 40 D. J. Groenendijk, M. Buscema, G. A. Steele, S. Michaelis de Vasconcellos, R. Bratschitsch, H. S. J. van der Zant and A. Castellanos-Gomez, *Nano Lett.*, 2014, **14**, 5846–5852.
- 41 D. Mac Donald, *Thermoelectricity: An Introduction to the Principles*, John Wiley & Sons, 1962.
- 42 N. Mott and H. Jones, *The theory of the properties of metals and alloys*, The Clarendon Press, 1936.
- 43 G. Nolas, J. Sharp and H. Goldsmid, *Thermoelectrics: Basic Principles and New Materials Developments*, Springer, 2001, pp. –.
- 44 Bhushan, *Springer Handbook of Nanotechnology*, 2007.
- 45 J. P. Heremans, V. Jovovic, E. S. Toberer, A. Saramat, K. Kurosaki, A. Charoenphakdee, S. Yamanaka and G. J. Snyder, *Science*, 2008, **321**, 554–557.
- 46 A. Slachter, F. L. Bakker, J.-P. Adam and B. J. van Wees, *Nat. Phys.*, 2010, **6**, 879–882.
- 47 Z. Li, M.-H. Bae and E. Pop, *Applied Physics Letters*, 2014, **105**, –.
- 48 J. Wu, H. Schmidt, K. K. Amara, X. Xu, G. Eda and B. Özyilmaz, *Nano Lett.*, 2014, **14**, 2730–2734.
- 49 X. Xu, N. M. Gabor, J. S. Alden, A. M. van der Zande and P. L. McEuen, *Nano Lett.*, 2009, **10**, 562–566.
- 50 N. M. Gabor, J. C. W. Song, Q. Ma, N. L. Nair, T. Taychatanapat, K. Watanabe, T. Taniguchi, L. S. Levitov and P. Jarillo-Herrero, *Science*, 2011, **334**, 648–652.
- 51 J. H. Seol, I. Jo, A. L. Moore, L. Lindsay, Z. H. Aitken, M. T. Pettes, X. Li, Z. Yao, R. Huang, D. Broido, N. Mingo, R. S. Ruoff and L. Shi, *Science*, 2010, **328**, 213–216.
- 52 K. L. Grosse, M.-H. Bae, F. Lian, E. Pop and W. P. King, *Nat Nano*, 2011, **6**, 287–290.
- 53 Z. Wang, R. Xie, C. T. Bui, D. Liu, X. Ni, B. Li and J. T. L. Thong, *Nano Lett.*, 2010, **11**, 113–118.
- 54 J. P. Small, K. M. Perez and P. Kim, *Phys. Rev. Lett.*, 2003, **91**, 256801–.
- 55 K. P. Pernstich, B. Rossner and B. Batlogg, *Nat Mater*, 2008, **7**, 321–325.
- 56 J. Fleurial, L. Gailliard, R. Triboulet, H. Scherrer and S. Scherrer, *Journal of Physics and Chemistry of Solids*, 1988, **49**, 1237–1247.
- 57 A. L. Bassi, A. Bailini, C. S. Casari, F. Donati, A. Mantegazza, M. Passoni, V. Russo and C. E. Bottani, *J. Appl. Phys.*, 2009, **105**, 124307–9.
- 58 F. Song, L. Wu and S. Liang, *Nanotechnology*, 2012, **23**, 085401.
- 59 R. Gardner, F. Sweatt and D. Tanner, *Journal of Physics and Chemistry of Solids*, 1963, **24**, 1183–1196.
- 60 T. Low, M. Engel, M. Steiner and P. Avouris, *Physical Review B*, 2014, **90**, 081408.
- 61 E. Flores, J. R. Ares, A. Castellanos-Gomez, M. Barawi, I. J. Ferrer and C. Sanchez, *Applied Physics Letters*, 2015, **106**, 022102.
- 62 P. L. Richards, *Journal of Applied Physics*, 1994, **76**, 1–24.
- 63 M. Freitag, T. Low, F. Xia and P. Avouris, *Nat. Photon.*, 2013, **7**, 53–59.
- 64 L. Vicarelli, M. Vitiello, D. Coquillat, A. Lombardo, A. Ferrari, W. Knap, M. Polini, V. Pellegrini and A. Tredicucci, *Nature Materials*, 2012, **11**, 865–871.
- 65 M. Engel, M. Steiner and P. Avouris, *Nano Lett.*, 2014, **14**, 6414–6417.
- 66 T. Low, A. S. Rodin, A. Carvalho, Y. Jiang, H. Wang, F. Xia and A. H. Castro Neto, *Phys. Rev. B*, 2014, **90**, 075434.
- 67 G. Konstantatos, M. Badioli, L. Gaudreau, J. Osmond, M. Bernechea, F. P. G. de Arquer, F. Gatti and F. H. Koppens, *Nature nanotechnology*, 2012, **7**, 363–368.
- 68 C.-H. Liu, Y.-C. Chang, T. B. Norris and Z. Zhong, *Nat Nano*, 2014, **9**, 273–278.
- 69 T. Mueller, F. Xia, M. Freitag, J. Tsang and P. Avouris, *Phys. Rev. B*, 2009, **79**, 245430.
- 70 P. Blake, E. W. Hill, A. H. C. Neto, K. S. Novoselov, D. Jiang, R. Yang, T. J. Booth and A. K. Geim, *Appl. Phys. Lett.*, 2007, **91**, 063124–3.
- 71 C. Casiraghi, A. Hartschuh, E. Lidorikis, H. Qian, H. Harutyunyan, T. Gokus, K. S. Novoselov and A. C. Ferrari, *Nano Lett.*, 2007, **7**, 2711–2717.
- 72 M. M. Furchi, A. Pospischil, F. Libisch, J. Burgdörfer and T. Mueller, *Nano Lett.*, 2014, **14**, 4785–4791.
- 73 A. Urich, K. Unterrainer and T. Mueller, *Nano Lett.*, 2011, **11**, 2804–2808.
- 74 Z. Yin, H. Li, H. Li, L. Jiang, Y. Shi, Y. Sun, G. Lu, Q. Zhang, X. Chen and H. Zhang, *ACS Nano*, 2012, **6**, 74–80.
- 75 O. Lopez-Sanchez, D. Lembke, M. Kayci, A. Radenovic and A. Kis, *Nat Nano*, 2013, **8**, 497–501.
- 76 G. Fiori, F. Bonaccorso, G. Iannaccone, T. Palacios, D. Neumaier, A. Seabaugh, S. K. Banerjee and L. Colombo, *Nat Nano*, 2014, **9**, 768–779.
- 77 B. Radisavljevic and A. Kis, *Nature materials*, 2013, **12**, 815–820.
- 78 S. Bertolazzi, J. Brivio and A. Kis, *ACS Nano*, 2011, **5**, 9703–9709.
- 79 J. Pu, Y. Yomogida, K.-K. Liu, L.-J. Li, Y. Iwasa and T. Takenobu, *Nano Lett.*, 2012, **12**, 4013–4017.
- 80 Q. He, Z. Zeng, Z. Yin, H. Li, S. Wu, X. Huang and H. Zhang, *Small*, 2012, **8**, 2994–2999.
- 81 H. S. Lee, S.-W. Min, Y.-G. Chang, M. K. Park, T. Nam, H. Kim, J. H. Kim, S. Ryu and S. Im, *Nano Lett.*, 2012, **12**, 3695–3700.
- 82 W. Choi, M. Y. Cho, A. Konar, J. H. Lee, G.-B. Cha, S. C. Hong, S. Kim, J. Kim, D. Jena, J. Joo and S. Kim, *Adv. Mater.*, 2012, **24**, 5832–5836.
- 83 M. Fontana, T. Deppe, A. K. Boyd, M. Rinzan, A. Y. Liu, M. Paranjape and P. Barbara, *Scientific Reports*, 2013, **3**, 1634.
- 84 D.-S. Tsai, K.-K. Liu, D.-H. Lien, M.-L. Tsai, C.-F. Kang, C.-A. Lin, L.-J. Li and J.-H. He, *ACS Nano*, 2013, **7**, 3905–3911.
- 85 C.-C. Wu, D. Jariwala, V. K. Sangwan, T. J. Marks, M. C. Hersam and L. J. Lauhon, *J. Phys. Chem. Lett.*, 2013, **4**, 2508–2513.
- 86 W. Zhang, J.-K. Huang, C.-H. Chen, Y.-H. Chang, Y.-J. Cheng and L.-J. Li, *Adv. Mater.*, 2013, **25**, 3456–3461.
- 87 F. Schedin, A. K. Geim, S. V. Morozov, E. W. Hill, P. Blake, M. I. Katsnelson and K. S. Novoselov, *Nat Mater*, 2007, **6**, 652–655.
- 88 H. Fang, S. Chuang, T. C. Chang, K. Takei, T. Takahashi and A. Javey, *Nano Lett.*, 2012, **12**, 3788–3792.
- 89 D. J. Late, B. Liu, H. S. S. R. Matte, V. P. Dravid and C. N. R. Rao, *ACS Nano*, 2012, **6**, 5635–5641.

- 90 S. Tongay, J. Zhou, C. Ataca, J. Liu, J. S. Kang, T. S. Matthews, L. You, J. Li, J. C. Grossman and J. Wu, *Nano Lett.*, 2013, **13**, 2831–2836.
- 91 N. Perea-López, Z. Lin, N. R. Pradhan, A. Iniguez-Rábago, A. L. Elías, A. McCreary, J. Lou, P. M. Ajayan, H. Terrones, L. Balicas and M. Terrones, *2D Materials*, 2014, **1**, 011004.
- 92 W. Kim, A. Javey, O. Vermesh, Q. Wang, Y. Li and H. Dai, *Nano Lett.*, 2003, **3**, 193–198.
- 93 S. Ghatak and A. Ghosh, *Applied Physics Letters*, 2013, **103**, 122103.
- 94 D.-S. Tsai, D.-H. Lien, M.-L. Tsai, S.-H. Su, K.-M. Chen, J.-J. Ke, Y.-C. Yu, L.-J. Li and J.-H. He, *Selected Topics in Quantum Electronics, IEEE Journal of*, 2014, **20**, 30–35.
- 95 N. Kaushik, A. Nipane, F. Basheer, S. Dubey, S. Grover, M. M. Deshmukh and S. Lodha, *Applied Physics Letters*, 2014, **105**, –.
- 96 F. Xia, T. Mueller, R. Golizadeh-Mojarad, M. Freitag, Y.-m. Lin, J. Tsang, V. Perebeinos and P. Avouris, *Nano Lett.*, 2009, **9**, 1039–1044.
- 97 X. Cai, A. B. Sushkov, R. J. Suess, M. M. Jadidi, G. S. Jenkins, L. O. Nyakiti, R. L. Myers-Ward, S. Li, J. Yan, D. K. Gaskill, T. E. Murphy, H. D. Drew and M. S. Fuhrer, *Nat Nano*, 2014, **9**, 814–819.
- 98 N. D. Boscher, C. J. Carmalt, R. G. Palgrave, J. J. Gil-Tomas and I. P. Parkin, *Chemical Vapor Deposition*, 2006, **12**, 692–698.
- 99 Y.-H. Chang, W. Zhang, Y. Zhu, Y. Han, J. Pu, J.-K. Chang, W.-T. Hsu, J.-K. Huang, C.-L. Hsu and M.-H. Chiu, *ACS nano*, 2014, **8**, 8582–8590.
- 100 X. Lu, M. I. B. Utama, J. Lin, X. Gong, J. Zhang, Y. Zhao, S. T. Pantelides, J. Wang, Z. Dong and Z. Liu, *Nano letters*, 2014, **14**, 2419–2425.
- 101 J. C. Shaw, H. Zhou, Y. Chen, N. O. Weiss, Y. Liu, Y. Huang and X. Duan, *Nano Research*, 2014, **7**, 1–7.
- 102 G. W. Shim, K. Yoo, S.-B. Seo, J. Shin, D. Y. Jung, I.-S. Kang, C. W. Ahn, B. J. Cho and S.-Y. Choi, *ACS nano*, 2014, **8**, 6655–6662.
- 103 M. I. B. Utama, X. Lu, D. Zhan, S. T. Ha, Y. Yuan, Z. Shen and Q. Xiong, *Nanoscale*, 2014, **6**, 12376–12382.
- 104 X. Wang, Y. Gong, G. Shi, W. L. Chow, K. Keyshar, G. Ye, R. Vajtai, J. Lou, Z. Liu and E. Ringe, *ACS nano*, 2014, **8**, 5125–5131.
- 105 J. Xia, X. Huang, L. Liu, M. Wang, L. Wang, B. Huang, D. Zhu, J. J. Li, C.-Z. Gu and X. Meng, *Nanoscale*, 2014.
- 106 A. Abderrahmane, P. J. Ko, T. V. Thu, S. Ishizawa, T. Takamura and A. Sandhu, *Nanotechnology*, 2014, **25**, 365202–.
- 107 B. W. H. Baugher, H. O. H. Churchill, Y. Yang and P. Jarillo-Herrero, *Nat Nano*, 2014, **9**, 262–267.
- 108 A. Pospischil, M. M. Furchi and T. Mueller, *Nat Nano*, 2014, **9**, 257–261.
- 109 N. Perea-López, A. L. Elías, A. Berkdemir, A. Castro-Beltran, H. R. Gutiérrez, S. Feng, R. Lv, T. Hayashi, F. López-Urías, S. Ghosh, B. Muchharla, S. Talapatra, H. Terrones and M. Terrones, *Adv. Funct. Mater.*, 2013, **23**, 5511–5517.
- 110 N. Huo, S. Yang, Z. Wei, S.-S. Li, J.-B. Xia and J. Li, *Sci. Rep.*, 2014, **4**, 5209.
- 111 W. Zhang, M.-H. Chiu, C.-H. Chen, W. Chen, L.-J. Li and A. T. S. Wee, *ACS nano*, 2014.
- 112 V. Podzorov, M. E. Gershenson, C. Kloc, R. Zeis and E. Bucher, *Applied Physics Letters*, 2004, **84**, 3301–3303.
- 113 S. Das and J. Appenzeller, *Applied Physics Letters*, 2013, **103**, 103501.
- 114 J.-K. Huang, J. Pu, C.-L. Hsu, M.-H. Chiu, Z.-Y. Juang, Y.-H. Chang, W.-H. Chang, Y. Iwasa, T. Takenobu and L.-J. Li, *ACS Nano*, 2013, **8**, 923–930.
- 115 M. Tosun, S. Chuang, H. Fang, A. B. Sachid, M. Hettick, Y. Lin, Y. Zeng and A. Javey, *ACS Nano*, 2014, **8**, 4948–4953.
- 116 H.-J. Chuang, X. Tan, N. J. Ghimire, M. M. Perera, B. Chamlagain, M. M.-C. Cheng, J. Yan, D. Mandrus, D. Tomnek and Z. Zhou, *Nano Lett.*, 2014, **14**, 3594–3601.
- 117 A. Allain and A. Kis, *ACS Nano*, 2014, **8**, 7180–7185.
- 118 J. S. Ross, P. Klement, A. M. Jones, N. J. Ghimire, J. Yan, M. G., T. Taniguchi, K. Watanabe, K. Kitamura, W. Yao, D. H. Cobden and X. Xu, *Nat Nano*, 2014, **9**, 268–272.
- 119 P. Hu, Z. Wen, L. Wang, P. Tan and K. Xiao, *ACS Nano*, 2012, **6**, 5988–5994.
- 120 D. J. Late, B. Liu, J. Luo, A. Yan, H. Matte, M. Grayson, C. Rao and V. P. Dravid, *Advanced Materials*, 2012, **24**, 3549–3554.
- 121 H. Liu and P. Ye, *Electron Device Letters, IEEE*, 2012, **33**, 546–548.
- 122 P. Hu, L. Wang, M. Yoon, J. Zhang, W. Feng, X. Wang, Z. Wen, J. C. Idrobo, Y. Miyamoto, D. B. Geohegan and K. Xiao, *Nano Lett.*, 2013, **13**, 1649–1654.
- 123 R. B. Jacobs-Gedrim, M. Shanmugam, N. Jain, C. A. Durcan, M. T. Murphy, T. M. Murray, R. J. Matyi, R. L. Moore and B. Yu, *ACS Nano*, 2013, **8**, 514–521.
- 124 G. W. Mudd, S. A. Svatek, T. Ren, A. Patané, O. Makarovskiy, L. Eaves, P. H. Beton, Z. D. Kovalyuk, G. V. Lashkarev, Z. R. Kudrynskiy and A. I. Dmitriev, *Adv. Mater.*, 2013, **25**, 5714–5718.
- 125 S. Lei, L. Ge, S. Najmaei, A. George, R. Kappera, J. Lou, M. Chhowalla, H. Yamaguchi, G. Gupta and R. Vajtai, *ACS nano*, 2014, **8**, 1263–1272.
- 126 S. R. Tamalampudi, Y.-Y. Lu, R. Kumar U., R. Sankar, C.-D. Liao, K. Moorthy B., C.-H. Cheng, F. C. Chou and Y.-T. Chen, *Nano Lett.*, 2014, **14**, 2800–2806.
- 127 V. Capozzi and M. Montagna, *Phys. Rev. B*, 1989, **40**, 3182–3190.
- 128 O. Alekperov, M. Godjaev, M. Zarbaliev and R. Suleimanov, *Solid State Communications*, 1991, **77**, 65–67.
- 129 M. Genut, L. Margulis, G. Hodes and R. Tenne, *Thin Solid Films*, 1992, **217**, 91–97.
- 130 L. Plucinski, R. L. Johnson, B. J. Kowalski, K. Kopalko, B. A. Orłowski, Z. D. Kovalyuk and G. V. Lashkarev, *Phys. Rev. B*, 2003, **68**, 125304.
- 131 C. H. Ho and S. L. Lin, *Journal of Applied Physics*, 2006, **100**, 083508.
- 132 J. F. Sánchez-Royo, J. Pellicer-Porres, A. Segura, V. Muñoz Sanjosé, G. Tobías, P. Ordejón, E. Canadell and Y. Huttel, *Phys. Rev. B*, 2002, **65**, 115201.
- 133 C. H. d. Groot and J. S. Moodera, *Journal of Applied Physics*, 2001, **89**, 4336–4340.
- 134 J. F. Sánchez-Royo, A. Segura, O. Lang, E. Schaar, C. Pettenkofer, W. Jaegermann, L. Roa and A. Chevy, *Journal of Applied Physics*, 2001, **90**, 2818–2823.
- 135 R. Sreekumar, R. Jayakrishnan, C. Sudha Kartha, K. P. Vijayakumar, S. A. Khan and D. K. Avasthi, *Journal of Applied Physics*, 2008, **103**, –.
- 136 F. Liu, H. Shimotani, H. Shang, T. Kanagasekaran, V. Zólyomi, N. Drummond, V. I. Fal'ko and K. Tanigaki, *ACS Nano*, 2013, **8**, 752–760.
- 137 D. De, J. Manongdo, S. See, V. Zhang, A. Guloy and H. Peng, *Nanotechnology*, 2013, **24**, 025202.
- 138 Y. Tao, X. Wu, W. Wang and J. Wang, *Journal of Materials Chemistry C*, 2014.
- 139 G. Su, V. G. Hadjiev, P. E. Loya, J. Zhang, S. Lei, S. Maharjan, P. Dong, P. M. Ajayan, J. Lou and H. Peng, *Nano Lett.*, 2015, **15**, 506–513.
- 140 J. O. Island, M. Buscema, M. Barawi, J. M. Clamagirand, J. R. Ares, C. Sánchez, I. J. Ferrer, G. A. Steele, H. S. J. van der Zant and A. Castellanos-Gomez, *Advanced Optical Materials*, 2014, **2**, 641–645.
- 141 W.-W. Xiong, J.-Q. Chen, X.-C. Wu and J.-J. Zhu, *J. Mater. Chem. C*, 2014, **2**, 7392–7395.
- 142 Y.-R. Tao, X.-C. Wu and W.-W. Xiong, *Small*, 2014, **10**, 4905–4911.
- 143 A. Castellanos-Gomez, M. Buscema, R. Molenaar, V. Singh, L. Janssen, H. S. J. van der Zant and G. A. Steele, *2D Materials*, 2014, **1**, 011002–.
- 144 W. Schairer and M. W. Shafer, *phys. stat. sol. (a)*, 1973, **17**, 181–184.
- 145 A. Morita, *Applied Physics A*, 1986, **39**, 227–242.
- 146 Y. Akahama, S. Endo and S.-i. Narita, *J. Phys. Soc. Jpn.*, 1983, **52**, 2148–2155.
- 147 A. Castellanos-Gomez, L. Vicarelli, E. Prada, J. O. Island, K. L. Narasimha-Acharya, S. I. Blanter, D. J. Groenendijk, M. Buscema, G. A. Steele, J. V. Alvarez, H. W. Zandbergen, J. J. Palacios and H. S. J. van der

- Zant, *2D Materials*, 2014, **1**, 025001.
- 148 M. Buscema, D. J. Groenendijk, S. I. Blanter, G. A. Steele, H. S. J. van der Zant and A. Castellanos-Gomez, *Nano Lett.*, 2014, **14**, 3347–3352.
- 149 M. Buscema, D. J. Groenendijk, G. A. Steele, H. S. van der Zant and A. Castellanos-Gomez, *Nat Commun*, 2014, **5**, 4651.
- 150 F. Xia, H. Wang and Y. Jia, *Nat Commun*, 2014, **5**, 4458.
- 151 H. Liu, A. T. Neal, Z. Zhu, Z. Luo, X. Xu, D. Tománek and P. D. Ye, *ACS Nano*, 2014, **8**, 4033–4041.
- 152 J. Qiao, X. Kong, Z.-X. Hu, F. Yang and W. Ji, *Nat Commun*, 2014, **5**, –.
- 153 L. Li, Y. Yu, G. J. Ye, Q. Ge, X. Ou, H. Wu, D. Feng, X. H. Chen and Y. Zhang, *Nat Nano*, 2014, **9**, 372–377.
- 154 S. P. Koenig, R. A. Doganov, H. Schmidt, A. H. Castro Neto and B. Özyilmaz, *Applied Physics Letters*, 2014, **104**, 103106.
- 155 V. Tran, R. Soklaski, Y. Liang and L. Yang, *Phys. Rev. B*, 2014, **89**, 235319.
- 156 N. Youngblood, C. Chen, S. J. Koester and M. Li, *Nat Photon*, 2015, **advance online publication**, –.
- 157 A. Ortiz-Conde, F. J. García Sánchez and J. Muci, *Solid-State Electronics*, 2000, **44**, 1861–1864.
- 158 T. Hong, B. Chamlagain, W. Lin, H.-J. Chuang, M. Pan, Z. Zhou and Y.-Q. Xu, *Nanoscale*, 2014, **6**, 8978–8983.
- 159 O. Lopez-Sanchez, E. Alarcon Llado, V. Koman, A. Fontcuberta i Morral, A. Radenovic and A. Kis, *ACS Nano*, 2014, **8**, 3042–3048.
- 160 H. Li, X. Duan, X. Wu, X. Zhuang, H. Zhou, Q. Zhang, X. Zhu, W. Hu, P. Ren and P. Guo, *Journal of the American Chemical Society*, 2014, **136**, 3756–3759.
- 161 C. Dean, A. Young, I. Meric, C. Lee, L. Wang, S. Sorgenfrei, K. Watanabe, T. Taniguchi, P. Kim and K. Shepard, *Nature Nanotechnology*, 2010, **5**, 722–726.
- 162 G. F. Schneider, V. E. Calado, H. Zandbergen, L. M. Vandersypen and C. Dekker, *Nano letters*, 2010, **10**, 1912–1916.
- 163 X. Song, M. Oksanen, M. A. Sillanpää, H. Craighead, J. Parpia and P. J. Hakonen, *Nano letters*, 2011, **12**, 198–202.
- 164 P. Zomer, S. Dash, N. Tombros and B. Van Wees, *Applied Physics Letters*, 2011, **99**, 232104.
- 165 F. Bonaccorso, A. Lombardo, T. Hasan, Z. Sun, L. Colombo and A. C. Ferrari, *Materials Today*, 2012, **15**, 564–589.
- 166 O. Lopez-Sanchez, D. Dumcenco, E. Charbon and A. Kis, *arXiv preprint arXiv:1411.3232*, 2014.
- 167 Y. Li, C.-Y. Xu, J.-Y. Wang and L. Zhen, *Sci. Rep.*, 2014, **4**, –.
- 168 S. Chuang, R. Kapadia, H. Fang, T. C. Chang, W.-C. Yen, Y.-L. Chueh and A. Javey, *Applied Physics Letters*, 2013, **102**, 242101.
- 169 W. J. Yu, Y. Liu, H. Zhou, A. Yin, Z. Li, Y. Huang and X. Duan, *Nat Nano*, 2013, **8**, 952–958.
- 170 K. Roy, M. Padmanabhan, S. Goswami, T. P. Sai, G. Ramalingam, S. Raghavan and A. Ghosh, *Nat Nano*, 2013, **8**, 826–830.
- 171 W. Zhang, C.-P. Chuu, J.-K. Huang, C.-H. Chen, M.-L. Tsai, Y.-H. Chang, C.-T. Liang, Y.-Z. Chen, Y.-L. Chueh, J.-H. He, M.-Y. Chou and L.-J. Li, *Sci. Rep.*, 2014, **4**, 3826.
- 172 G.-H. Lee, C.-H. Lee, A. M. van der Zande, M. Han, X. Cui, G. Arefe, C. Nuckolls, T. F. Heinz, J. Hone and P. Kim, *APL Materials*, 2014, **2**, 092511.
- 173 C.-H. Lee, G.-H. Lee, A. M. van der Zande, W. Chen, Y. Li, M. Han, X. Cui, G. Arefe, C. Nuckolls, T. F. Heinz, J. Guo, J. Hone and P. Kim, *Nat Nano*, 2014, **9**, 676–681.
- 174 H. Fang, C. Battaglia, C. Carraro, S. Nemsak, B. Ozdol, J. S. Kang, H. A. Bechtel, S. B. Desai, F. Kronast, A. A. Unal, G. Conti, C. Conlon, G. K. Palsson, M. C. Martin, A. M. Minor, C. S. Fadley, E. Yablonovitch, R. Maboudian and A. Javey, *Proceedings of the National Academy of Sciences*, 2014, **111**, 6198–6202.
- 175 N. Huo, J. Kang, Z. Wei, S.-S. Li, J. Li and S.-H. Wei, *Adv. Funct. Mater.*, 2014, **24**, 7025–7031.
- 176 Y. Gong, J. Lin, X. Wang, G. Shi, S. Lei, Z. Lin, X. Zou, G. Ye, R. Vajtai, B. I. Yakobson, H. Terrones, M. Terrones, B.-K. Tay, J. Lou, S. T. Pantelides, Z. Liu, W. Zhou and P. M. Ajayan, *Nat Mater*, 2014, **13**, 1135–1142.
- 177 Y. Deng, Z. Luo, N. J. Conrad, H. Liu, Y. Gong, S. Najmaei, P. M. Ajayan, J. Lou, X. Xu and P. D. Ye, *ACS Nano*, 2014, **8**, 8292–8299.
- 178 S. Wi, M. Chen, H. Nam, A. C. Liu, E. Meyhofer and X. Liang, *Applied Physics Letters*, 2014, **104**, 232103.
- 179 C. H. Lui, Z. Ye, C. Ji, K.-C. Chiu, C.-T. Chou, T. I. Andersen, C. Means-Shively, H. Anderson, J.-M. Wu and T. Kidd, *arXiv preprint arXiv:1410.4224*, 2014.
- 180 H. Fang, C. Battaglia, C. Carraro, S. Nemsak, B. Ozdol, J. S. Kang, H. A. Bechtel, S. B. Desai, F. Kronast and A. A. Unal, *Proceedings of the National Academy of Sciences*, 2014, **111**, 6198–6202.
- 181 J. He, N. Kumar, M. Z. Bellus, H.-Y. Chiu, D. He, Y. Wang and H. Zhao, *Nature communications*, 2014, **5**, 5622.
- 182 Y. Yu, S. Hu, L. Su, L. Huang, Y. Liu, Z. Jin, A. A. Puzosky, D. B. Geohegan, K. W. Kim, Y. Zhang and L. Cao, *Nano Lett.*, 2015, **15**, 486–491.
- 183 X. Hong, J. Kim, S.-F. Shi, Y. Zhang, C. Jin, Y. Sun, S. Tongay, J. Wu, Y. Zhang and F. Wang, *Nat Nano*, 2014, **9**, 682–686.
- 184 S. Tongay, W. Fan, J. Kang, J. Park, U. Koldemir, J. Suh, D. S. Narang, K. Liu, J. Ji, J. Li, R. Sinclair and J. Wu, *Nano Lett.*, 2014, **14**, 3185–3190.
- 185 F. Ceballos, M. Z. Bellus, H.-Y. Chiu and H. Zhao, *ACS Nano*, 2014, **8**, 12717–12724.
- 186 K. Liu, Q. Yan, M. Chen, W. Fan, Y. Sun, J. Suh, D. Fu, S. Lee, J. Zhou and S. Tongay, *Nano Letters*, 2014, **14**, 5097–5103.
- 187 A. M. van der Zande, P. Y. Huang, D. A. Chenet, T. C. Berkelbach, Y. You, G.-H. Lee, T. F. Heinz, D. R. Reichman, D. A. Muller and J. C. Hone, *Nat Mater*, 2013, **12**, 554–561.
- 188 Y. Zhang, Y. Zhang, Q. Ji, J. Ju, H. Yuan, J. Shi, T. Gao, D. Ma, M. Liu, Y. Chen, X. Song, H. Y. Hwang, Y. Cui and Z. Liu, *ACS Nano*, 2013, **7**, 8963–8971.
- 189 C. Cong, J. Shang, X. Wu, B. Cao, N. Peimyoo, C. Qiu, L. Sun and T. Yu, *Advanced Optical Materials*, 2014, **2**, 131–136.
- 190 H. Zhou, C. Wang, J. C. Shaw, R. Cheng, Y. Chen, X. Huang, Y. Liu, N. O. Weiss, Z. Lin, Y. Huang and X. Duan, *Nano Lett.*, 2015, **15**, 709–713.
- 191 J. Huang, L. Yang, D. Liu, J. Chen, Q. Fu, Y. Xiong, F. Lin and B. Xiang, *Nanoscale*, 2015, **7**, 4193–4198.
- 192 Y. Shi, H. Li and L.-J. Li, *Chem. Soc. Rev.*, 2015, DOI:10.1039/C4CS00256C.
- 193 Q. Ji, Y. Zhang, Y. Zhang and Z. Liu, *Chem. Soc. Rev.*, 2015, DOI:10.1039/C4CS00258J.
- 194 M.-H. Chiu, M.-Y. Li, W. Zhang, W.-T. Hsu, W.-H. Chang, M. Terrones, H. Terrones and L.-J. Li, *ACS Nano*, 2014, **8**, 9649–9656.
- 195 A. M. van der Zande, J. Kunstmann, A. Chernikov, D. A. Chenet, Y. You, X. Zhang, P. Y. Huang, T. C. Berkelbach, L. Wang and F. Zhang, *Nano letters*, 2014, **14**, 3869–3875.
- 196 W.-T. Hsu, Z.-A. Zhao, L.-J. Li, C.-H. Chen, M.-H. Chiu, P.-S. Chang, Y.-C. Chou and W.-H. Chang, *ACS Nano*, 2014, **8**, 2951–2958.
- 197 M. Okada, T. Sawazaki, K. Watanabe, T. Taniguchi, H. Hibino, H. Shinohara and R. Kitaura, *ACS Nano*, 2014, **8**, 8273–8277.
- 198 H. Ago, H. Endo, P. Solís-Fernández, R. Takizawa, Y. Ohta, Y. Fujita, K. Yamamoto and M. Tsuji, *ACS Appl. Mater. Interfaces*, 2015, **7**, 5265–5273.
- 199 X. Zhang, F. Meng, J. R. Christianson, C. Arroyo-Torres, M. A. Lukowski, D. Liang, J. R. Schmidt and S. Jin, *Nano Lett.*, 2014, **14**, 3047–3054.
- 200 D. Kufer, I. Nikitskiy, T. Lasanta, G. Navickaite, F. H. L. Koppens and G. Konstantatos, *Adv. Mater.*, 2015, **27**, 176–180.

- 201 G. Eda and S. A. Maier, *ACS Nano*, 2013, **7**, 5660–5665.
- 202 J. Miao, W. Hu, Y. Jing, W. Luo, L. Liao, A. Pan, S. Wu, J. Cheng, X. Chen and W. Lu, *Small*, 2015, DOI:10.1002/sml.201403422.
- 203 J. Lin, H. Li, H. Zhang and W. Chen, *Applied Physics Letters*, 2013, **102**, 203109.
- 204 S. Najmaei, A. Mlayah, A. Arbouet, C. Girard, J. Léotin and J. Lou, *ACS Nano*, 2014, **8**, 12682–12689.
- 205 X. Gan, R.-J. Shiue, Y. Gao, I. Meric, T. F. Heinz, K. Shepard, J. Hone, S. Assefa and D. Englund, *Nat Photon*, 2013, **7**, 883–887.
- 206 X. Wang, Z. Cheng, K. Xu, H. K. Tsang and J.-B. Xu, *Nat Photon*, 2013, **7**, 888–891.
- 207 H. Li, Y. Anugrah, S. J. Koester and M. Li, *Applied Physics Letters*, 2012, **101**, 111110.
- 208 X. Liu, T. Galfsky, Z. Sun, F. Xia, E.-c. Lin, Y.-H. Lee, S. Kena-Cohen and V. M. Menon, *Nat Photon*, 2015, **9**, 30–34.
- 209 S. Wu, S. Buckley, A. M. Jones, J. S. Ross, N. J. Ghimire, J. Yan, D. G. Mandrus, W. Yao, F. Hatami, J. Vuckovic, A. Majumdar and X. Xu, *2D Materials*, 2014, **1**, 011001.
- 210 S. Wu, S. Buckley, J. R. Schaibley, L. Feng, J. Yan, D. G. Mandrus, F. Hatami, W. Yao, J. Vuckovic, A. Majumdar and X. Xu, *Nature*, 2015, **advance online publication**, –.
- 211 S. Schwarz, S. Dufferwiel, P. M. Walker, F. Withers, A. A. P. Trichet, M. Sich, F. Li, E. A. Chekhovich, D. N. Borisenko, N. N. Kolesnikov, K. S. Novoselov, M. S. Skolnick, J. M. Smith, D. N. Krizhanovskii and A. I. Tartakovskii, *Nano Lett.*, 2014, **14**, 7003–7008.
- 212 A. Klots, A. Newaz, B. Wang, D. Prasai, H. Krzyzanowska, D. Caudel, N. Ghimire, J. Yan, B. Ivanov and K. Velizhanin, *arXiv preprint arXiv:1403.6455*, 2014.
- 213 D. Akinwande, N. Petrone and J. Hone, *Nat Commun*, 2014, **5**, 5678.
- 214 W. Zhu, M. N. Yogeesh, S. Yang, S. H. Aldave, J.-S. Kim, S. Sonde, L. Tao, N. Lu and D. Akinwande, *Nano Lett.*, 2015, **15**, 1883–1890.
- 215 T. Georgiou, R. Jalil, B. D. Belle, L. Britnell, R. V. Gorbachev, S. V. Morozov, Y.-J. Kim, A. Gholinia, S. J. Haigh, O. Makarovskiy, L. Eaves, L. A. Ponomarenko, A. K. Geim, K. S. Novoselov and A. Mishchenko, *Nat Nano*, 2013, **8**, 100–103.
- 216 Y. Zhou, Y. Nie, Y. Liu, K. Yan, J. Hong, C. Jin, Y. Zhou, J. Yin, Z. Liu and H. Peng, *ACS Nano*, 2014, **8**, 1485–1490.
- 217 M. Amani, R. A. Burke, R. M. Proie and M. Dubey, *Nanotechnology*, 2015, **26**, 115202.
- 218 Y. Sun, S. Gao and Y. Xie, *Chem. Soc. Rev.*, 2014, **43**, 530–546.
- 219 G. Chen, Y. Yu, K. Zheng, T. Ding, W. Wang, Y. Jiang and Q. Yang, *Small*, 2015, DOI: 10.1002/sml.201403508.
- 220 A. Nathan, A. Ahnood, M. T. Cole, S. Lee, Y. Suzuki, P. Hiralal, F. Bonaccorso, T. Hasan, L. Garcia-Gancedo and A. Dyadyusha, *Proceedings of the IEEE*, 2012, **100**, 1486–1517.
- 221 F. Withers, O. Del Pozo-Zamudio, A. Mishchenko, A. P. Rooney, A. Gholinia, K. Watanabe, T. Taniguchi, S. J. Haigh, A. K. Geim, A. I. Tartakovskii and K. S. Novoselov, *Nat Mater*, 2015, **14**, 301–306.

Abbreviation	Description
TMDCs	Transition metal dichalcogenides
bP	Black phosphorus
FET	Field-effect transistor
I_{ds}	Source-drain current
I_{ds}	Source-drain current
V_g	Gate voltage
PC	Photoconductance
PG	Photogating
PV	Photovoltaic
PTE	Photothermoelectric
SBs	Schottky Barriers
SPCM	Scanning photocurrent microscopy
I_{sc}	Short-circuit current
V_{oc}	Open-circuit voltage
P_{el}	Electrical power
CVD	Chemical vapour deposition

Table 3 List of abbreviations.

12 List of abbreviations

13 Appendix: Tables

Material	Measurement conditions				Responsivity R (mA W ⁻¹)	Rise time τ (ms)	Spectral range	Reference
	V_{ds} (V)	V_g (V)	λ (nm)	P (mW cm ⁻²)				
1L MoS ₂	1	50	532	8.0×10^4	7.5	5×10^1	Visible	74
1L MoS ₂	8	-70	561	2.4×10^{-1}	8.8×10^5	6×10^2	Visible	75
1L MoS ₂ ^c	1	41	532	1.3×10^{-1}	2.2×10^6	5×10^5	-	86
1L MoS ₂	1.5	0	514.5	3.2×10^4	1.1	1×10^4	-	91
>1L MoS ₂	1	-2	633	5.0×10^1	1.1×10^2	1×10^3	Visible - NIR	82
2L MoS ₂	5	100	WL _a	5 nW	6.2×10^5	2×10^4	-	34
3L MoS ₂	10	0	532	2.0×10^3	5.7×10^2	7.0×10^{-2}	$\lambda < 700$ nm	84
1L MoSe ₂	10	0	532	1×10^2	1.3×10^1	6×10^1	-	105
1L MoSe ₂	1	0	650	5.9×10^2	2.6×10^{-1}	2.5×10^1	-	99
20L MoSe ₂	20	0	532	4.8	9.7×10^4	3.0×10^1	-	106
1L WS ₂ ^c	30	0	458	2.0	2.1×10^{-2}	5.3	Visible	109
1L WS ₂ ^c	30	0	633	5.0×10^{-2}	1.3×10^4	2.0×10^1	-	110
1L WSe ₂	2	-60	650	3.8×10^{-1}	1.8×10^5	1.0×10^4	-	111
1L WSe ₂	0	PN	WL _a	4.5×10^1	1.0×10^1	-	-	108
1L WSe ₂	0	PN	522	1×10^{-2}	8.4×10^{-1}	-	$\lambda < 820$ nm	107
1L WSe ₂	0	PN	532	8.4×10^{-1}	4×10^{-1}	1.0×10^1	$\lambda < (770 \pm 35)$ nm	40

a. WL = white light. b. Power in W. c. Data reported for the device in vacuum.

Table 4 Figures-of-merit for MoS₂, MoSe₂, WS₂ and WSe₂ based photodetectors

Material	Measurement conditions				Responsivity R (mA W ⁻¹)	Rise time τ (ms)	Spectral range	Reference
	V_{ds} (V)	V_g (V)	λ (nm)	P (mW cm ⁻²)				
TiS ₃	1	-40	640	3×10^{-1}	2.9×10^6	4	$\lambda < 1100$ nm	140
ZrS ₃	5	-	405	5×10^{11}	5×10^{-2}	13×10^3	$\lambda < 850$ nm	142
HfS ₃	5	-	405	1.2	1.1×10^2	4×10^2	$\lambda < 650$ nm	141

Table 5 Figures-of-merit for TiS₃, ZrS₃ and HfS₃ based photodetectors

Material	Measurement conditions				Responsivity R (mA W ⁻¹)	Rise time τ (ms)	Spectral range	Reference
	V_{ds} (V)	V_g (V)	λ (nm)	P (mW cm ⁻²)				
GaTe	5	0	532	3.0×10^{-5}	1×10^7	6	Visible	136
GaSe	5	0	254	1.0	2.8×10^3	3×10^2	UV - Visible	119
GaS	2	0	254	2.6×10^{-2}	4.2×10^3	3×10^1	UV - Visible	122
In ₂ Se ₃	5	0	300	2.1×10^{-1}	3.9×10^5	1.8×10^1	UV - NIR	123
InSe	10	80	633	3.5×10^2	1.6×10^5	4.0×10^3	Visible - NIR	126
InSe	3	0	532	2.5×10^2	3.5×10^1	5.0×10^{-1}	Visible - NIR	125
SnS ₂	3	0	457	2×10^3	9	5×10^{-3}	Visible - NIR	139

Table 6 Figures-of-merit for photodetectors based on III-VI compounds

Thickness (nm)	Measurement conditions				Responsivity R (mA W ⁻¹)	Rise time τ (ms)	Spectral range	Reference
	V_{ds} (V)	V_g (V)	λ (nm)	P (mW cm ⁻²)				
8	0.2	0	640	1.6×10^1	4.8	1	Visible - NIR	148
6	0	PN	532	1.9×10^3	5×10^{-1}	1.5	Visible - NIR	149
6	-0.5	PN	532	1.9×10^3	2.8×10^1	-	Visible - IR	149
120	0	0	1550	3×10^6	5.0	-	Visible - IR	65,66
120	0	0	532	1×10^7	2.0×10^1	-	Visible - NIR	65,66
11.5	0.4	-8	1550	1.91	1.3×10^2	a	Visible - NIR	156 ^b

a. $f_{3dB} = 3$ GHz b. Power in mW.

Table 7 Figures-of-merit for few-layer bP based photodetectors